The Superconducting Super Proton Synchrotron

First Year Design Report

Luke Dyks, David Posthuma de Boer, Aimee Ross
University of Oxford

Michael Backhouse
Imperial College London

Siobhan Alden, Gian Luigi D'Alessandro, Daniel Harryman
Royal Holloway, University of London

March 2019

Edited by Luke Dyks and David Posthuma de Boer

Abstract and introduction by Luke Dyks.

Lattice design chapter by Siobahn Alden and Gian Luigi D'Alessandro.

Magnet design chapter by Luke Dyks, Michael Backhouse and Daniel Harryman.

RF cavity design chapter by David Posthuma de Boer and Aimee Ross.

Conclusion by Luke Dyks and David Posthuma de Boer

John Adams Institute for Accelerator Science 2019.

Abstract

In order to continue pushing the frontiers of high energy physics, a future circular hadron collider, FCC-*hh* has been proposed. Using 16 T magnets the FCC-*hh* will be able to collide two beams of hadrons with a centre of mass energy of order 100 TeV [1]. In doing so it is hoped that FCC-*hh* will shed light on some of the mysteries of modern particle physics, in particular the nature of the Higgs potential and the Standard Model of Particle Physics as well as what may lie beyond.

An important consideration for the design of the FCC-*hh* is the series of accelerators that will be used to inject the hadron beams into the collider. The FCC-*hh* requires a high energy injector. One possible machine to be used for this purpose is the superconducting Super Proton Synchrotron, scSPS [2]. The scSPS is a new superconducting accelerator that will be built in the same tunnel as the normal conducting, Super Proton Synchrotron, SPS. The scSPS will be able to accelerate proton beams to an energy of 1.3 TeV, nearly three times as high as the SPS, for extraction to either the FCC-*hh* or to fixed target experiments.

This report details the results of a design study for such an upgrade with a focus on the lattice design, magnet design and RF cavity design. A recommended design for a dispersion suppressor is discussed and the cell dimensions optimised to fit in the existing SPS tunnel. Preliminary designs for the magnets are proposed. Three superconducting designs are proposed for both the dipole and quadrupole magnets. These designs provide the freedom to operate the scSPS at 4.2 K with double layered magnets and 1.9 K with single layered magnets. The design of both superconducting and normal conducting sextupole magnets for chromaticity corrections have also been produced. A superconducting RF cavity design is also presented, requiring state-of-the-art high bandwidth, and fast tuners.

Acknowledgements

The work undertaken in this report would not have been possible without the help of many of our colleagues.

First and foremost we would like to thank Emmanuel Tsesmelis and Suzie Sheehy, not only for their invaluable input in this project, but for leading the introductory accelerator course at the John Adams Institute.

We would also like to thank Ciprian Plostinar for the input he provided on RF cavity design in the tutorial he gave and in our weekly meetings. The tutorial given to us by Attilio Milanese on magnet design was also invaluable. Finally we would like to extend our thanks to Léon Van Riesen-Haupt, for his support and guidance on lattice design and knowledge of the FCC study.

Contents

1 Introduction

1.1 The Future Circular Collider Project

The Large Hadron Collider, LHC, is the largest and most powerful particle accelerator in the world [3]. Conceived in the 1980s and built between 1998 - 2008, the LHC is a synchrotron that can accelerate two beams of protons to a centre of mass energy of 13 TeV or heavy ions to a centre of mass energy of 5 TeV. In operation the LHC has contributed greatly to the field of particle physics, leading to the discovery of the Higgs boson in 2012[4, 5], as well as providing detailed measurements of the properties of other Standard Model, SM, particles. However, the LHC, and its upgrade, the high luminosity LHC, HL-LHC, will not be able to explore the entire Standard Model, such as the precise nature of the Higgs particle. The LHC may also fail to provide an answer to what lies beyond the Standard Model, so called BSM physics. Some BSM problems include the nature of Dark Matter, the origin of neutrino masses and the origin of matter-antimatter asymmetry. A new higher energy and higher precision collider may help us to solve these problems.

The Future Circular Collider, FCC, has been proposed for this purpose [6]. There are three potential configurations of the FCC, each to be situated in a 100 km circular tunnel at the CERN site. The first stage would be to build an e^+/e^- collider, FCC-*ee*, with reach a centre of mass energy of 400 GeV. The second stage would be to reuse the tunnel and build a hadron collider, which could be followed by an electron-hadron collider.

A proton-proton FCC-*hh* built with 16 T dipole magnets could produce collisions with a centre of mass energy of 100 TeV [1, 6]. The integrated luminosity of such a collider is expected to be $\sim 20\,\mathrm{ab}^{-1}$ over a period of $\sim$ 20 years, corresponding to the production of over 10 billion Higgs bosons and over 1 trillion top quarks. FCC-*hh* could also be used to accelerate lead ions to a centre of mass energy of 39 TeV. With this centre of mass energy and luminosity the FCC-*hh* should be able to produce particles up to a mass of 43 TeV, proving the existence or not of any BSM particles, such as supersymmetric particles, that lie below that mass.

1.2 Physics at FCC-*hh*

1.2.1 The Higgs Potential

More progress is expected to be made in exploring the Higgs' properties during the operation of HL-LHC and FCC-*ee* [6]. However, neither will be able to probe one of the Higgs' most significant properties, how it couples to itself. Uncovering the answer would vastly increase our knowledge of Higgs potential parameters. These are fixed in the Standard Model, but could be affected by BSM processes. Analysis of these parameters could shed light on the electroweak phase transition that occurred at $\sim 10 \times 10^{-10}\,\mathrm{s}$ after the Big Bang and may provide an explanation for the origin of matter-antimatter asymmetry. The FCC-*hh* is targeted to be able to tell us if the expectation value for this transition deviates from the Standard Model to a precision of 5%, around ten times higher precision than for HL-LHC.

1.2.2 Dark Matter

Despite observing the effect of Dark Matter on a galactic scale, virtually nothing is known about its properties [6]. Several competing theories have been proposed to explain the nature of Dark Matter, from heavy black holes to particles with masses lower than those of neutrinos. One suggested model is that Dark Matter is made of weakly interacting massive particles, WIMPS, which have masses around the 1-3 TeV range. Since they are predicted to couple very weakly to Standard Model particles, the LHC can only directly produce WIMPS at a fraction of their mass range. The FCC-*hh* should be able to cover the rest of the WIMP mass range and, if they exist, provide evidence for them.

1.2.3 New Physics Through Indirect Evidence

Direct production of new particles is not the only way that the FCC-*hh* could provide evidence for BSM physics [6]. Before particles such as the top quark or the W and Z bosons were directly discovered, their existence was strongly inferred through indirect evidence collected in colliders.

Likewise, precision measurements of processes in the FCC-*ee* may hint at the existence of particles of mass a few TeV. Particles of this mass are beyond other accelerators currently envisaged and could only be confirmed by the FCC-*hh*.

1.3 FCC-*hh* Injector Options

In order to reduce construction costs it will be necessary to reuse as much of the current CERN accelerator complex as possible for the FCC-*hh*. There are three options for the final high energy booster, HEB, that will inject particles into the FCC-*hh* ring, re-purposing the LHC as a booster, installing a normal conducting iron based HEB in the FCC-*hh* tunnel or installing a superconducting accelerator in the SPS tunnel, the so called scSPS[7]. The HEB must be able to fill 80 % of the FCC ring with protons, corresponding to 10,400 bunches of 1×10^{11} protons spaced by 25 ns. This must be done in a time of ~ 30 minutes. These proton beams must have of order TeV energy and a normalised emittance of 2.2 μm.

The current baseline for FCC-*hh* injection is that protons are injected from the LHC at an energy of 3.3 TeV. In this scheme the injection chain to be used for the HL-LHC (LINAC4, Booster, PS, SPS) would be re-purposed with the LHC undergoing several design changes [6]. Firstly it would be necessary to replace two of the beam crossover points, currently used by the ALICE and LHCb experiments, to make room for extractions towards the FCC. To be able to satisfy the filling time for the FCC, the ramp rate of the LHC must be increased by a factor 5. The current restriction on the ramp rate of the LHC is the maximum ramp rate of the main dipole magnets, so these must be upgraded if the LHC is to be used as a HEB for the FCC. Another design issue for the LHC as a HEB is that the transfer lines from the LHC tunnel to the FCC would require at least 4 km of superconducting magnets. The LHC is also a complex machine to operate, meaning running costs could be high and long maintenance delays could be necessary.

Another option is to house an accelerator with 1 T, superferric dipole magnets in the FCC tunnel itself to inject into the FCC at an energy of 3.3 TeV [7]. This would be able to provide the required number of bunches in a shorter time than the LHC. However, due to its large circumference, this design would require a high power RF system, similar to the one used in the LHC. Furthermore, the beam in the superferric HEB could interact with the beam in FCC-*hh* creating large amounts of background radiation at experiments. This may require separate bypass tunnels to be dug around the FCC-*hh* experiments.

The third option currently being considered for an injector into the FCC-*hh* is upgrading the SPS to the scSPS [2, 6]. The upgrade provides several advantages over other HEB schemes. The scSPS will be able to fill the FCC-*hh* in a faster time than the LHC, but not as fast as the superferric 1 T HEB. Using the scSPS would reduce the overall complexity of the injector chain. This would consist of 4 accelerators (LINAC4, Booster, PS, scSPS), rather than 5 accelerators for the other two options. The scSPS will be relatively simple to operate when compared with the LHC, and would be expected to reduce operating costs. Since the scSPS will inject at a lower energy to the LHC-HEB, normal conducting transfer lines can be used to transport the beam from booster to the FCC-*hh*. The injection from the scSPS into the FCC-*hh* would also be safer than injection from the LHC-HEB due to the lower energy of the transported beams. This would again reduce the cost and complexity of the FCC-*hh* machine protection system. The main parameters of the three HEB options are listed in Table 1.

Parameter	Unit	LHC	1 T Superferric	scSPS
Circumference	km	26.7	100	6.9
Injection Energy	Gev	450	450	25
Extraction energy	TeV	3.3	3.3	1.3
Number of dipoles		1232	~ 1000	372
Number of quadrupoles		480	~ 1000	216
Injection field	T	0.6	0.14	0.12
Extraction field	T	4	1	6
Magnet ramp rate	T/s	0.035	0.01	0.5
FCC filling time	min	43	32	41
Stored energy per beam	MJ	140	560	13

Table 1: Main parameter of the current HEB options for the FCC-*hh*.

If it is decided that CERN will not build the FCC-*hh*, the scSPS could also be used as an injector to a high energy upgrade to the LHC, the HE-LHC. It would be advantageous to use the scSPS for this purpose as it would reduce the energy swing in the HE-LHC, and would improve the field quality and aperture of HE-LHC [2].

Whilst not being used as an injector for FCC-*hh* or HE-LHC, the scSPS could provide high energy and intensity beams for fixed target experiments in the CERN North Area. Fast extraction of the beam to the North Area could be useful for physics experiments, especially for the testing of materials in a high radiation environment. Most fixed target experiments, however, require a high integrated proton rate which can only be achieved through slow extraction of the beam, over a time period of a few hundred milliseconds to a few seconds. Slow extracted beams would be available for a similar amount of time as the current SPS beams for fixed target experiments. The beams would have $\sim 5 \times 10^{13}$ protons per cycle and could deliver $\sim 1 \times 10^{19}$ protons on target per year.

1.4 Super Proton Synchrotron

The Super Proton Synchrotron, SPS, was designed in the late 1960s by a team led by Sir John Adams [8]. Operation began in 1976 at a proton beam energy of 400 GeV [9]. In 1981 the SPS was converted into a proton anti-proton collider, the S$p\bar{p}$S [9]. Operation of the S$p\bar{p}$S led to the discover of the W and Z bosons in 1983. Between 1989 and 2000 the SPS was used in the injection chain for the Large Electron Positron collider, LEP [10]. It is currently used to inject protons and lead ions into the LHC at an energy of 450 GeV and provide proton beams to several fixed target experiments [3].

The SPS is housed in a 6.9 km circumference tunnel and uses 744 normal conducting dipole magnets, with a maximum field strength of 2 T to steer the beam. 216 quadrupole magnets are used in the SPS to focus the beam, each providing a maximum field gradient of 22 T/m. In 1972 it was proposed that the SPS should use superconducting magnets [11]. The proposal suggested using 4.5 T dipole magnets in the tunnel to reach an energy of 1 TeV. However, this was dropped because the superconducting magnets available at the time could not ramp at a fast enough time to be used in a synchrotron.

1.5 Design Considerations for scSPS

Some preliminary studies have been undertaken for design of the scSPS and are detailed in [2], the main parameters of which are displayed in Table 2. The scSPS will share the same tunnel as the current SPS, and so will keep most of the SPS tunnel geometry [2]. The tunnel is split into six long straight sections, LSSs, and six bending sections, shown in Figure 1. If possible, the LSS functionalities will be kept identical to those of the SPS. Therefore, in the scSPS, LSS1 is where the beam will be injected, LSS2 is where slow extraction to the CERN North Area will take place, LSS3 is where the RF system will be located, LSS4 and LSS6 is for fast extraction to the FCC-*hh* and LSS5 is where the collimation system will be. LSS6 will also contain the beam dump.

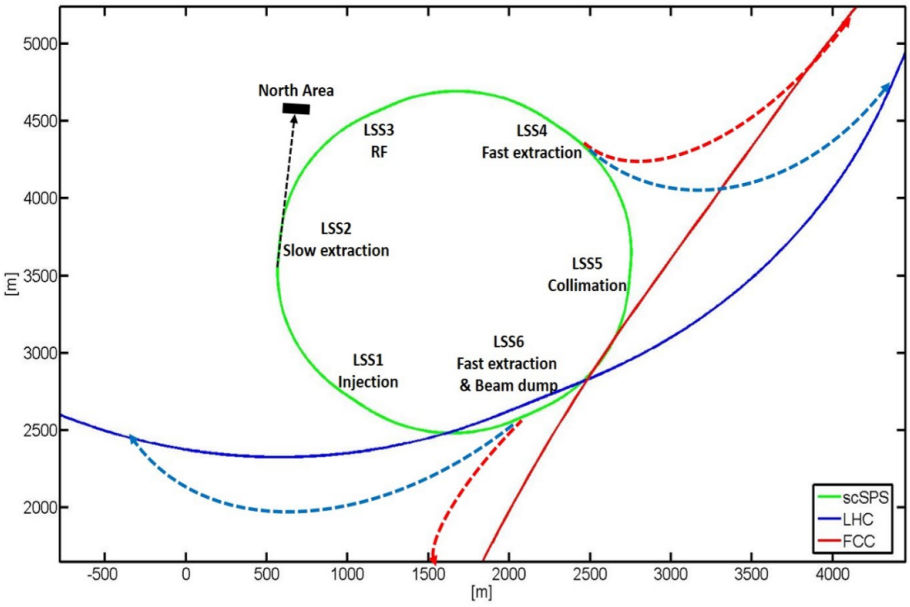

Figure 1: The layout of the scSPS. Showing the positions of the LSSs of the scSPS, the LHC, the FCC and the transfer lines from the scSPS to the other two accelerators [6].

The current design of the scSPS has 372 dipole magnets, each 12.2 m in length. The dipoles will be superconducting and have a maximum field strength of 6 T. To focus the beam the scSPS will have 216 quadrupoles, each 1.35 m in length with a maximum magnetic field gradient of 146.25 T/m. The injector to the scSPS is assumed to be the existing Proton Synchrotron, PS, which will inject at an energy of 25 GeV corresponding to a dipole field of 0.12 T. The scSPS will accelerate the beam to an energy of 1.3 TeV, when it will be extracted to the FCC-*hh*. It is important to note that the swing in magnet field strength is ~ 50, which may prove impractical. If this is the case then a higher energy injector into the scSPS, based around the PS2 accelerator [12], could be used. This would increase the injection energy to the scSPS to 50 GeV and reduce the magnetic swing by a factor 2.

As mentioned in Section 1.3, in order to be considered as an injector to the FCC-*hh*, the scSPS must be able to fill 80 % of the FCC-*hh* ring, 10,400 proton bunches, in ~ 30 minutes. A nearly full scSPS can accelerate 640 bunches in one cycle, from 8 injections from the PS [2]. The scSPS can, therefore, transfer the 320 bunches to each FCC-*hh* beam per cycle. In order to achieve the filling time for the FCC-*hh*, each scSPS cycle must take place is ~ 1 minute, which requires a maximum ramp rate of ~ 0.5 T/s in the dipoles.

The aperture required for the scSPS is fixed by the beam parameters at injection [2]. The normalised emittance, $\epsilon_{x,y}$ was assumed to be equal to the beam emittance allowed in the FCC-*hh*, 2.2 μm, which was then used to calculate the beam size to $\pm 10\ \sigma$, allowing for a factor 1.21 for optics imperfections. Including the maximum dispersion of the beam further increases the required aperture. To compensate for misalignment of the beam an extra factor, $O_{x,y} = \pm 2.5$ mm, was included. Injection oscillations also increase the size of the required aperture by a factor $I_{x,y} = \pm 1.5$ mm. The minimum aperture needed for these conditions is given by

$$A_{x,y}/2 = |O_{x,y}| + |I_{x,y}| + 10\sqrt{1.21\beta_{x,y}\epsilon_{x,y}} + 1.1|D_{x,y}|\delta p/p, \tag{1}$$

into which the initial design values for the scSPS from Table 2 are substituted. This gives a required diameter of 80 mm. This is a reasonably large value for a high energy accelerator and could cause issues for the magnet design. A 50 GeV injection energy from the PS2 would reduce the required diameter to 70 mm.

Parameter	**Unit**	**scSPS**
Circumference	m	6900
Dipole Bending Radius	m	723
Injection Energy	GeV	25
Maximum Energy	GeV	1300
Minimum Dipole Field	T	0.12
Maximum Dipole Field	T	6
Number of Dipoles		372
Number of Quadrupoles		216
Ramp Rate	T/s	0.35 - 0.5
Number of Bunches per Fill		640
Number of Protons per Bunch		$\leq 2.5 \times 10^{11}$
Dipole Length	m	12.12
Half Cell Length	m	32
Dipoles per Cell		4
Quadrupole Gradient	T/m	146.25
Maximum Beta Function	m	107
Maximum Dispersion	m	4.3
Normalised Emittance $\epsilon_{x,y}$	μm	2.2
$\delta p/p$		5×10^{-4}

Table 2: The baseline parameters for the scSPS as detailed in [2].

2 Lattice

A version of the lattice configuration for the scSPS has already been studied and proposed by the FCC collaboration [2]. Studies in this section will follow at first this implemented model and propose at a latter stage, possible geometrical and cell length optimisations together with first studies for sextupoles, chromaticity and dispersion suppressors.

2.1 SPS and scSPS Parameters

Initial parameters for the scSPS lattice were obtained from the previously proposed configuration by the FCC collaboration; these are listed in Table 3. As the scSPS is to use the same tunnel as the SPS, the FCC Collaboration study proposed to use the same cell length as the existing SPS lattice, $L_{cell} = 64\,\mathrm{m}$. With this cell length the phase advance per cell for the scSPS is $\mu = 89.96\,^\circ$. The FCC Collaboration study also listed dipole lengths of both 12 m and 12.12 m, with a field strength of 6 T. Using these parameters as starting points, the focal length, F_Q, for the quadrupoles was calculated as per

$$F_Q = \frac{L_{cell}}{4 \sin \frac{\mu}{2}} \tag{2}$$

where L_{cell} is the length of the cell. The focal length can also be defined as

$$F_Q = \frac{1}{k_1 l_Q} \tag{3}$$

where k_1 is the quadrupole strength, and l_Q is the quadrupole length [13]. Equation 3 was used with the length from Table 3 to obtain $k_1 = 0.033\,\mathrm{m}^{-2}$. This was then used to model one arc of the scSPS; the full ring is then made from six repetitions of this arc using MADX. A plot of the β_x, β_y and dispersion are shown in Figure 2.

Parameter	**Unit**	**SPS**	**scSPS**
Extraction Energy	GeV	450	1300
Length of Cell	m	64	64
Dipole Length	m	6.26	12.12
Number of Dipoles per Cell		8	4
Maximum Dipole Strength	T	2.02	6
Phase Advance per Cell	degree	71	89.96
β_{max}	m	107	107
Quadrupole Length	m	3.1	1.35
Quadrupole Focusing strength	m^{-2}	0.0112	0.033

Table 3: The current SPS lattice parameters compared to the initial scSPS lattice parameters.

The low dispersion region of Figure 2 is the location of the dispersion suppressor in the LSS, also called the interaction point (IP) for historical reasons. This area can be divided in six cells, two external with one missing dipoles and four internal with no dipoles (straight section). A different configuration of the dispersion suppressor leading to zero dispersion is shown in the next sections. The β functions in Figure 2 are in good agreement with the values in Table 3, having maximum value β of 107 m in both planes. The maximum dispersion as well does not exceed the maximum value of $\sim 4.5\,\mathrm{m}$.

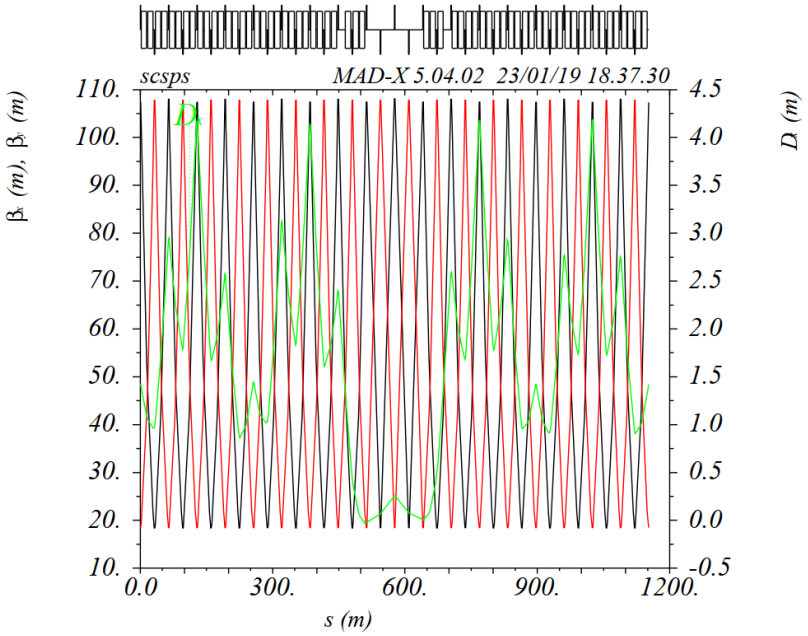

Figure 2: Output of MADX simulation of the scSPS lattice.

In order to have a direct comparison with the SPS the optics for one arc of this machine are shown in Figure 3. It can be seen that values for betas are comparable, with a major difference in the dispersion values (almost double compared to the one of the scSPS). This difference is given by the different dipole configuration.

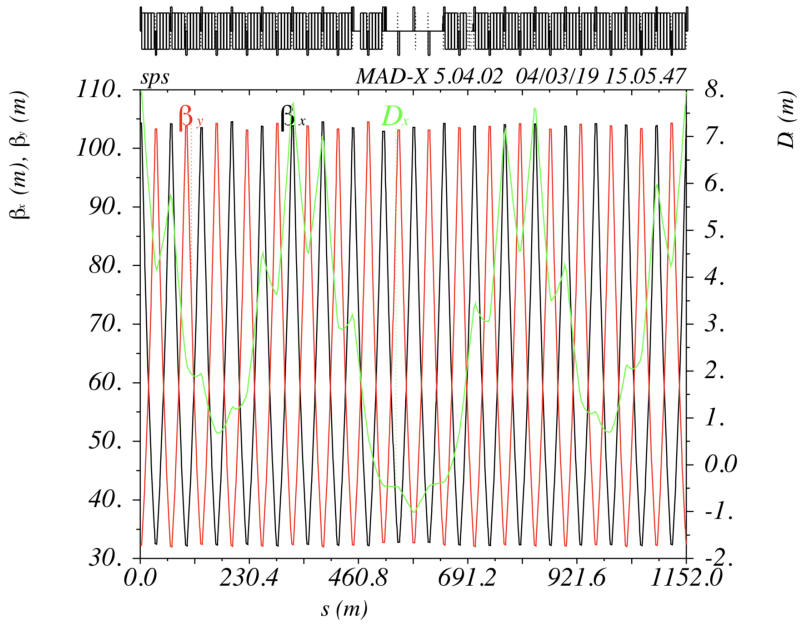

Figure 3: Output of MADX simulation of SPS lattice.

2.2 Chromaticity and Sextupole Parameters

For a given magnetic field gradient of a quadrupole magnet, particles with smaller momentum will feel a stronger focusing force. The chromaticity Q' describes an optical error of a quadrupole lens

in an accelerator. By definition, the chromaticity Q' for a ring of circumference, C is given by [13]:

$$Q' = -\frac{1}{4\pi}\int_0^C \beta(s)k(s)ds. \tag{4}$$

This value $Q' = -34.64$ can be compared with the value obtained from MADX $Q'_{\mathrm{madx}} = -35.30$. This quantity can be corrected with a sextupole scheme. The equation relating the chromaticity of the machine and the sextupoles field is

$$Q' = \frac{-1\int B''(s)\beta(s)D(s)ds}{4\pi B\rho}, \tag{5}$$

with B" being the sextupole field gradient. Considering a beampipe aperture of 40 mm radius the peak field is given by

$$B_{peak} = \frac{B''a^2}{2}, \tag{6}$$

which gives an average peak field of 0.2 T for the scSPS parameters. This value can be used as a first approximation for MADX simulations. These show that using a scheme with a sextupole after every quadrupole, sextupoles could easily cancel this effect, leading to a final chromaticity of 0.02. This value is low enough to keep the system away from resonances and lead to a stable chromaticity compensation.

2.3 Dispersion Suppressor Schemes

The design of the dispersion suppressor for the scSPS had not yet been proposed. This section aims at investigating three different methods that lead to zero dispersion in the LSSs. For an overview on dispersion suppressors, see [14]. These methods are:

1. Reduced field suppressor.
2. Singularly-powered quadrupoles.
3. Trimmer quadrupoles suppressor.

The reduced field suppressor leads to zero dispersion in the LSS by reducing the field of one of the dipoles in the region before the straight section. This method is particularly straightforward and alters the current geometry in one of the cells close to the dispersion suppressor.

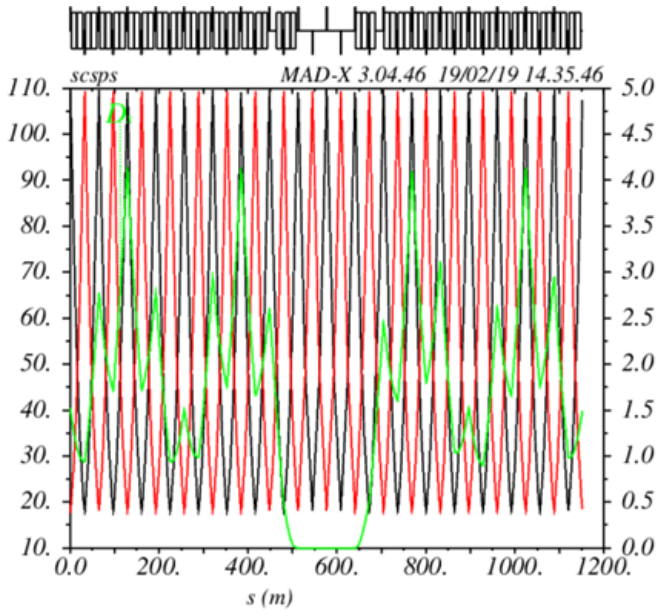

Figure 4: Reduced field suppressor

The singularly-powered quadrupole method alternates the strength of two quadrupoles which leads to stronger on-axis focusing. This method does not alter the geometry of the lattice but increases β_x by $\sim 10\,\%$.

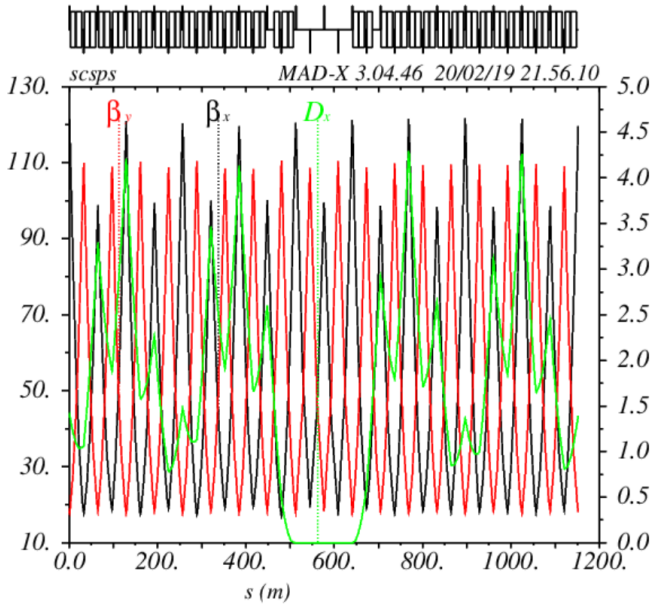

Figure 5: Singularly-powered quadrupoles suppressor

Finally, by adding trimmer quadrupoles it is possible to leave β_x and β_y in the arcs unchanged and to obtain large β functions only in the LSSs. This solution would not change most of the current scSPS lattice but would require extra insertions of quadrupoles.

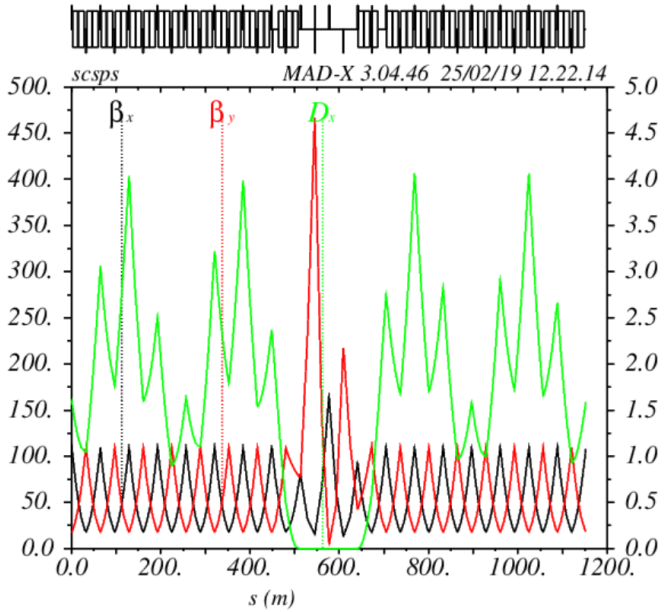

Figure 6: Trimmer quadrupoles suppressor

2.4 Matching the Tunnel Geometry

A major constraint for the scSPS is that the lattice must fit within the existing tunnel geometry for the SPS. To investigate this the optics for the scSPS were extended to model the full ring rather than one arc. A survey plot of the SPS, scSPS with 12 m dipoles, and scSPS with 12.12 m dipoles is shown in Figure 7.

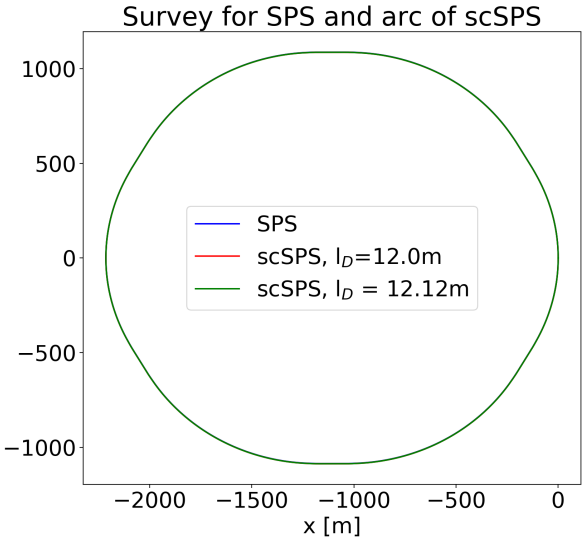

Figure 7: Survey ploy of SPS and two scSPS lattice configurations with 12 m and 12.12 m dipoles

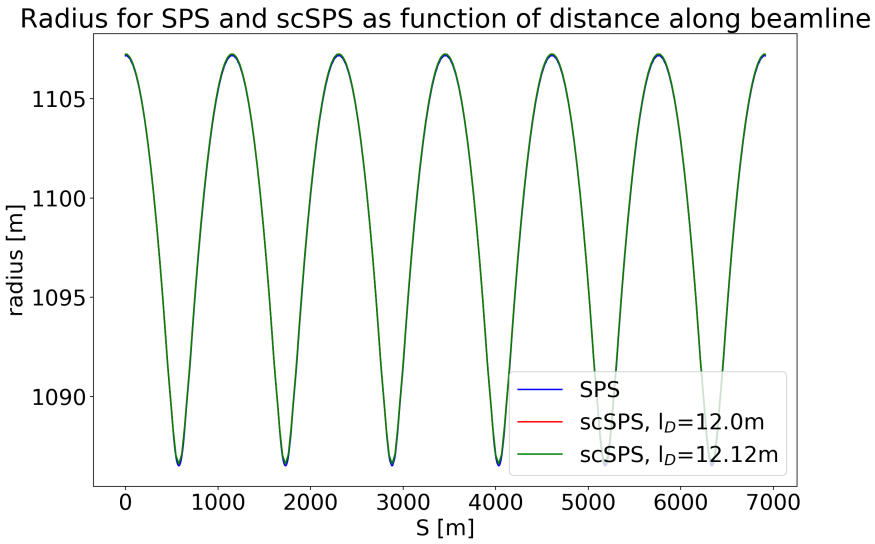

Figure 8: Radius of beam line for the SPS and the scSPS as a function of beam line position.

From the survey all options appear to be in good agreement, however, due to the strict constraint of the tunnel and a potential maximum deviation of 0.5 m from the existing beam line, further investigations were necessary. Plotting the radius, r, of the beam line for the SPS and scSPS configurations as a function of the distance along the beamline, S, Figure 8, reveals deviation between the two paths. The sinusoidal trend in radius plot is due to the combination of bending sections and drift sections in the lattice. The main deviation between the SPS beamline

and the scSPS beamlines occur at the peaks and troughs of the path, and are likely caused by the dispersion suppressor scheme used in these locations. The maximum deviation for both the 12 m and 12.12 m beam line is approximately 8 cm from that of the SPS. While this would require the beam line to be slightly re-positioned when compared to the SPS, it is well within the tolerance of 0.5 m from the SPS beam line.

2.5 Alternative Lattice Designs

All development made to this lattice was built on the original proposal to use the same cell length, 64 m, as the SPS. Further studies were made in order to ascertain if any alternative cell lengths would result in a viable lattice for the scSPS. In order to conduct this study a maximum and minimum circumference for the scSPS was set based upon a radius of ± 0.5 m of the existing 6912 m SPS circumference. Another limitation is found in the sinusoidal form revealed in the $r(S)$ distribution in Figure 8. Any alternative lattice would also need to follow the SPS beam line within the 0.5 m tolerance. The sinusoidal form is a result of the six repeating arcs, therefore, alternative lattice designs would also need six repeating arcs. Another consideration is the need to have an even number of cells per arc. To provide starting points for cell lengths to consider the maximum and minimum circumference can be seen in Figure 9, with the number of cells, N_{cell}, vs the cell length, L_{cell}. From this distribution an integer number of cells can be chosen and the resulting required cell length can be found within the maximum and minimum circumference lines.

We studied one smaller cell length, 57.6 m, and one larger cell length, 72 m. In both cases the drift distances between elements, and the quadrupole length, were kept the same as in the 64 m cell. The phase advance for any cell would also need to match the design value of $\mu = 89.96°$. As a result the parameters to be calculated for each alternative lattice are the dipole length, dipole strength, and quadrupole focusing strength.

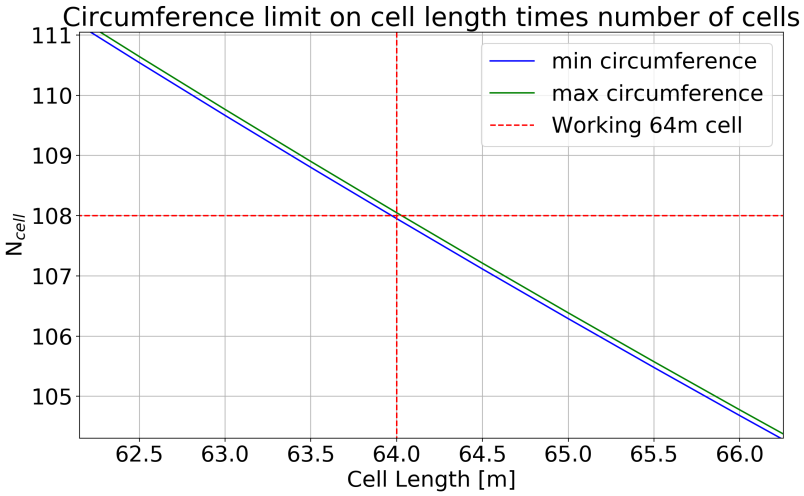

Figure 9: Number of cells with required cell length for maximum and minimum circumference's

To change the dipole length there are some considerations that need to be made to evaluate the impact on the field strength. The total number of dipoles in the full ring multiplied by their bending angle need to equal 2π. The bending angle is proportional to the dipole length through the following relation

$$\theta = \frac{Bl_D}{B\rho} \tag{7}$$

where θ is the dipole bending angle, B is the dipole field strength, l_D is the dipole length, and $B\rho$ is the magnetic rigidity. Using these relations a plot of the number of dipoles in the full ring against the dipole length was made over a range of magnetic field strengths, Figure 10.

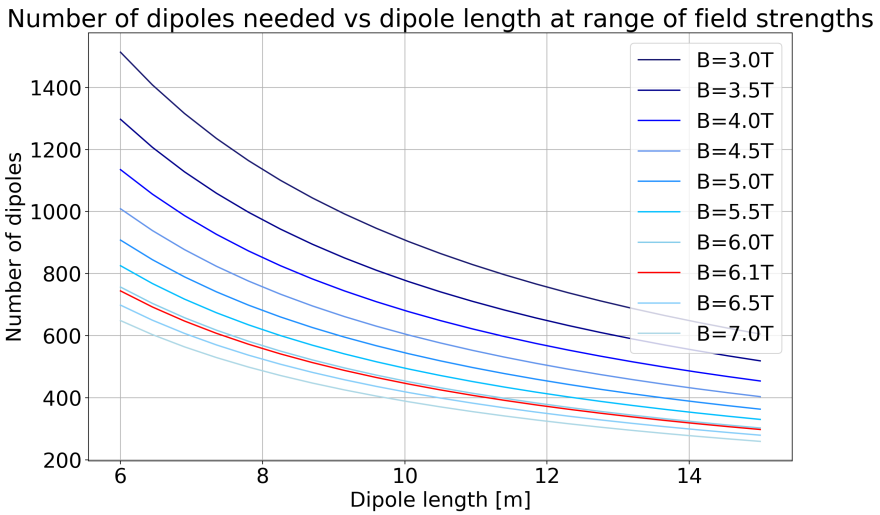

Figure 10: Number of dipoles required at different dipole lengths for fixed B fields

It was established that for the 57.6 m cell, dipoles would be 10.52 m in length but to reach the required bending angle would need to have a field strength of 6.16 T, which is higher than the 6 T field required for the 64 m cell design. For a 72 m cell the dipole length would be 14.12 m which is nearing the limit available for the necessary cryogenic cooling system to surround the dipole. However, a 14.12 m dipole would only require a field of 5.82 T.

Finally, it was also necessary to calculate the quadrupole focusing strengths for the alternative lattice designs. As both the phase advance and the quadrupole length were set to remain unchanged in all three considered cell lengths the quadrupole focusing strength is dictated by Equation 3, as the focal length is set by the phase advance. The resulting quadrupole focusing strengths for the 57.6 m and 72 m cells were calculated as $0.036\,\mathrm{m}^{-2}$ and $0.029\,\mathrm{m}^{-2}$ respectively. Once again the geometries of the alternative designs were compared with the current SPS beam line. Figure 11 shows the beam line radius for each lattice design along with the SPS beam line as a function of S, to identify any deviations. The 57.6 m cell length design has a maximum deviation of 0.5 m, located at the dispersion suppressor as in the 64 m cell length design. This deviation is on the edge of the tolerance for shifting the beam line and still fitting in the existing SPS tunnel. The 72 m cell length design has a maximum deviation of 1 m, also found at the dispersion suppressor, which is greater than the 0.5 m tolerance. However, with tuning of the element positions within the cell, these deviations could be reduced further.

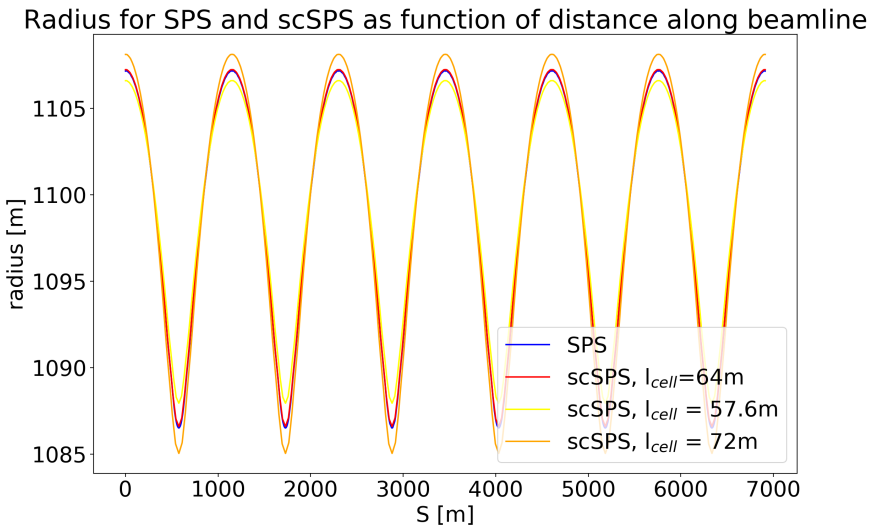

Figure 11: Radius of beam line for 3 lattice designs with 3 cell length options as a function of distance along beam line, S

$\mathbf{l_{cell}}$	$\mathbf{N_{cells}}$ **per arc**	$\mathbf{k_1}$	$\mathbf{l_{dipole}}$	$\mathbf{k_{dipole}}$	$\beta_{\mathbf{max}}$	**Max. offset from SPS**
57.6 m	20	$0.036\,\mathrm{m}^{-2}$	10.52 m	6.16 T	98 m	0.50 m
64.0 m	18	$0.033\,\mathrm{m}^{-2}$	12.12 m	6.00 T	107 m	0.08 m
72.0 m	16	$0.029\,\mathrm{m}^{-2}$	14.12 m	5.82 T	122 m	1.00 m

Table 4: Some of the parameters required for the three different cell lengths.

Table 4 lists the key parameters for all three considered lattice designs. Of these the 64 m deviates from the SPS beam line by a maximum of 0.08 m and only in the dispersion suppressor region. The 57.6 m cell length lattice is on the tolerance for the 0.5 m offset from the SPS beam line so is a viable option without further tuning. However, the 72 m cell length lattice design has a deviation from the SPS beam line of greater than the 0.5 m tolerance, so further development would be required before it could be used. With that in mind it is worth considering accelerator parameters for each lattice design. The shortest cell length lattice offers a reduction in the β_{max}, resulting in a reduction in the aperture, which is advantageous when designing the quadrupole magnets seen in Section 3.3. The main disadvantage of this design is the required increase in dipole field to 6.16 T. If the magnetic field strength becomes a primary concern, then the 72 m cell length design offers some reduction in these requirements. This, however, comes at the cost of an increase to 122 m for β_{max} and a deviation in the beam line outside the tunnel geometry constraints.

2.6 Outlook

Three dispersion suppressor schemes have been proposed for use in the scSPS. The advantages and disadvantages of these must be analysed in order to decide on the optimal design. Particular investigation must be made into the size of the beam pipe aperture needed for designs with different beta functions. Dispersion suppression design could also be carried out on the alternative lattices proposed in this section.

Although initial chromaticity correction studies have been undertaken these need to be developed further. By using a higher sextupole field, the number of sextupoles used in the lattice could be reduced, providing more room in the lattice for other equipment. Further to this, studies of chromaticity and the correction of chromaticity should be undertaken for each of the alternative lattice designs.

3 Magnets

3.1 Introduction

3.1.1 Magnets in the scSPS

Some of the most critical components of the design of the scSPS are the magnets. Designs needing to be produced for several different magnets, each with different purposes. It is necessary to design dipole magnets to bend the beam around the synchrotron, quadrupoles for focusing the beam and sextupoles for providing chromaticity corrections to the beam. In addition to these, octupole, kicker and corrector magnets must also be developed.

3.1.2 Electromagnetic Design

Charged particles moving through electromagnetic fields will experience a force, F, from the field [15]. This is known as the Lorentz force and is given by,

$$F = q(\mathbf{E} + \mathbf{v} \times \mathbf{B}), \tag{8}$$

where q is the charge of the particles, $\boldsymbol{v}$ is its velocity and $\boldsymbol{B}$ and $\boldsymbol{E}$ are the magnetic and electric fields the particle has passed through. Since particles in an accelerator tend to be moving at speeds close to the speed of light, we can use transverse magnetic fields to steer and guide the beam. Since accelerator magnets tend to be much longer than they are wide, the magnetic field can approximated as 2D [16, 15]. This 2D magnetic field can then be represented as a series expansion in terms of complex multipoles or harmonics. For a complex variable $z = x + iy$, where the x-y plane describes the cross section of a magnet, the magnetic field, $B_y + iB_x$, can be expressed as the series,

$$B_y(z) + iB_x(z) = \sum_{n=1}^{\infty}(B_n + iA_n)(\frac{z}{R})^{n-1}, \tag{9}$$

where the coefficients B_n and A_n are the normal and skew multipole terms of the magnetic field. A pure multipolar field has only a single non-zero coefficient. For example the term B_1 describes a pure dipole field and B_2 describes a pure quadrupole field and so on. The A_n terms describe skew multipolar terms of the n^{th} order.

If we take the expansion in x only, that is in the horizontal direction, and ignore the skew terms, we can evaluate the spacial profile of the multipole harmonics. The dipole term, B_1 has no x dependence and so is constant in space, meaning that the bending force seen by a particle is independent of its position in a perfect dipole magnet. The quadrupole term, B_2, has a linear variation in B_y with position, with a gradient, g. The central field of a perfect quadrupole is zero. It is this field profile that allows quadrupole magnets to focus beams. Particles at large distances from the magnet centre receive a larger inward force than particles at a smaller distance. The magnetic field perpendicular to B_y, B_x also has a linear dependence of position, with a gradient of the same magnitude but opposite sign, hence the quadrupole magnets focus in one plane and defocus in the other. The sextupole term, B_3 has a quadratic dependence on x, again with zero field at the magnet centre. The main characterisation of a sextupole magnet is the second derivative of field,

$$B'' = \frac{\partial^2 B_y}{\partial x^2} = \frac{2B_3}{R^2}. \tag{10}$$

As mentioned in Section 2, B_1, g and B'' are often normalised by the beam rigidity,

$$k_0 = \frac{B}{(B\rho)}, k_1 = \frac{g}{(B\rho)}, k_2 = \frac{B''}{(B\rho)}, \tag{11}$$

in order to give constant values during the ramp.

By calculating the series expansion for a magnet we can create a measure of magnetic field quality. Typically this is done over a good field region of 2/3 of the physical aperture radius. The expansion over this region for a well designed dipole magnet would contain a large B_1 term, with any higher harmonics representing small unwanted field distortions. Typically we normalise these

distortions by the wanted field component and multiply by 10,000. For example, the normalised unwanted quadrupole component in a dipole magnet, b_2, is given by,

$$b_2 = 10000\frac{B_2}{B_1}. \tag{12}$$

Typically these normalised distortions are denoted by lower case b_n and a_n and are in units of 10^{-4}. The same can be done for distortions on higher order multipole fields, again by normalising by the wanted magnetic component. When designing a magnet the geometry of a magnet can be altered to reduce the value of the unwanted harmonics. A common goal when designing a magnet is to reduce the harmonics to $\sim 10^{-4}$. Any misalignment of magnets could also introduce unwanted higher multipole or skew terms to the series expansion.

We can eliminate several of the unwanted harmonics by designing magnets to have certain symmetries. For example designing a dipole magnet with 2-fold symmetry, through both the x and y axis, will eliminate all even numbered harmonics, leaving only odd harmonics. For a quadrupole with 4-fold symmetry only the $B_2, B_6, B_{10}...$ harmonics are allowed and for a sextupole with 6 fold symmetry, only the $B_3, B_9, B_{15}...$ harmonics are allowed.

3.1.3 Superconducting Magnet Design

The magnetic fields required in the scSPS are far higher than can be achieved with resistive magnets. Therefore, both the dipole and quadrupole magnets must be made with superconducting material. Superconductivity, when electricity can flow through a material with zero resistance, was first discovered in mercury, cryogenically cooled to 4.2 K, in 1911[16]. The first superconducting accelerator magnets were produced in the early 1970s [16] and have been used extensively since. The first accelerator to be based around superconducting magnets was the Tevatron, which used 4.5 T dipoles and quadrupoles with a pole tip field of 2.8 T to achieve beam energies of 980 GeV, over twice that of the normal conducting SPS.

For superconducting material to become superconducting it must be cooled to low temperatures. The temperature at which a material becomes superconducting is known as the critical temperature, T_c, if its temperature is raised higher than this, the material will quench and become normal conducting. A superconductor will also quench if the current density flowing through it is too high. The current density at which this occurs is know as the critical current density, j_c. There is also a maximum magnetic field that a superconducting can experience before it quenches, known as the critical field, B_c. The value of the current density, magnetic field and temperature, effect the values of j_c, B_c and Tc. We, therefore, define a critical surface that the superconductor must operate below in order to remain superconducting. Two slices through this surface, one at 4.2 K and one at 1.9 K, can be seen in Figure 12 for niobium-titanium, NbTi, superconductor. The temperatures 4.2 K and 1.9 K are important, as they can be achieved by cooling with liquid helium or superfluid helium respectively.

The cost of this cooling must be taken into account when designing an accelerator. As superconducting magnets have zero electrical resistance, they only use a small amount of power compared to resistive magnets. The cost of the electricity to run a superconducting magnet is, therefore, much lower. Despite this, the overall running costs of superconducting magnets are significantly higher than resistive magnets. The reason for the cost is the cryogenic cooling one must use in operation. Running at a temperature of 1.9 K is more expensive than running at 4.2 K, which again must be considered.

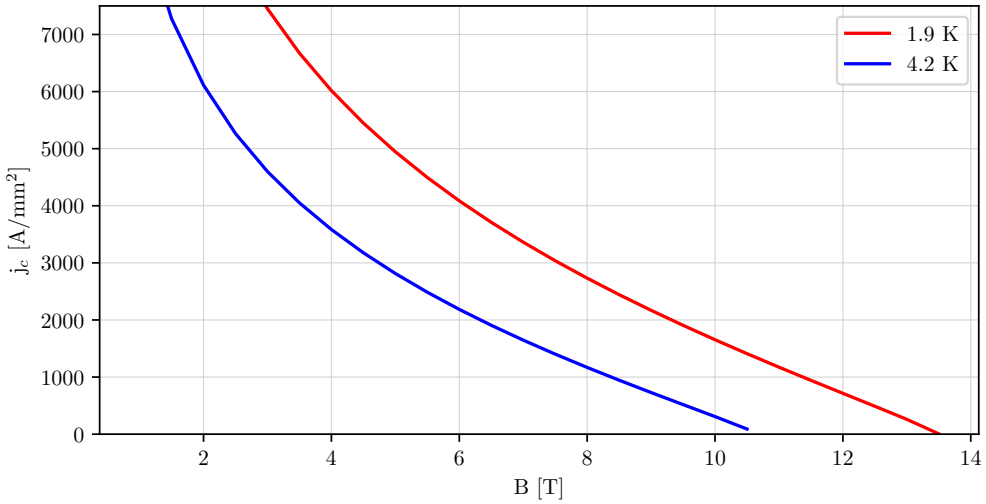

Figure 12: The critical current density at different magnetic field strengths for NbTi superconducting cables at 4.2 K and 1.9 K, calculated using [17].

The most common type of superconductor used in accelerator magnets is NbTi which was discovered in 1961 [16]. The critical temperature for NbTi is 9.2 K. It was used in the LHC to produce dipole magnets that had a central field of 8.36 T when cooled to 1.9 K. NbTi cables are relatively easy to produce and the material is relatively cheap. For the HL-LHC upgrade, new magnets used in the final focus have been designed, made from niobium-tin, Nb_3Sn. The critical temperature for Nb_3Sn, is 18.2 K and may be able to produce reliable 16 T dipole fields for the FCC-*hh*. Although the field that can be maintained in Nb_3Sn is very high the material is difficult to make into cables and is brittle. The cost is also several times higher than NbTi. So called high temperature superconductors, HTS, do exist. HTSs are able to operate at temperatures that can be produced using liquid nitrogen as a coolant, however, these are far from use in particle accelerator magnets.

To avoid quenches in localised areas which can cause the entire magnet to quench, solid blocks of pure superconductor are not used in accelerator magnets. Instead individual strands of superconductor are embedded in a copper stabiliser, as shown in Figure 13. If one of the individual strands quenches locally, the copper acts to conduct the current that would otherwise heat the wire causing further quenches. For use in an accelerator magnet several of these wires are woven together to create a Rutherford cable, Figure 13. The cable can be wound round the magnet yoke several times to form a coil block.

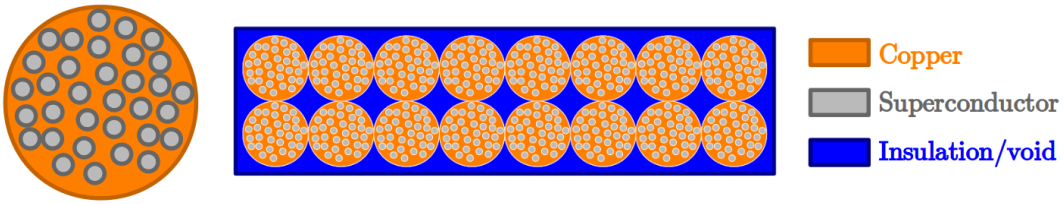

Figure 13: A diagram of a typical superconducting wire with several strands suspended in a copper stabiliser (left). A diagram of the cross section of a Rutherford cable (right).

The geometry of the coil blocks are essential to the design of the magnet. It can be shown [15], that if current is distributed around the axis at the centre of a magnet aperture in a $\cos(\theta)$ distribution, then the magnet will have a pure dipole field. A $\cos(\theta)$ distribution can be approxi-

mated by placing coil blocks around the magnet with spacers in between. Such magnets are very common in particle accelerators and are know as $\cos(\theta)$ magnets. It can also be shown that a pure quadrupole field is produced when the coil blocks are positioned to replicate a $\cos(2\theta)$ distribution of current. Such magnets are known as $\cos(2\theta)$ magnets.

3.1.4 SIS300 Fast Ramping Magnets

One of the challenges involved with designing the magnets for the scSPS is the high ramp rate required. Most current superconducting accelerator magnets ramp at a much lower rate than the 0.5 T/s rate required in the scSPS. For example the current LHC magnets operate at a ramp rate of $\sim 7 - 8$ mT/s [3]. The SIS300 is a fast ramping synchrotron being developed to accelerate heavy ions for the Facility for Anti-proton and Ion Research, FAIR, at GSI in Germany [18]. For SIS300, superconducting dipole and quadrupole magnets have been designed, reaching magnetic ramp rates of ~ 1 T/s. For these designs, particular focus was placed on reducing AC losses, providing good conductor cooling and maintaining acceptable field quality during the ramp.

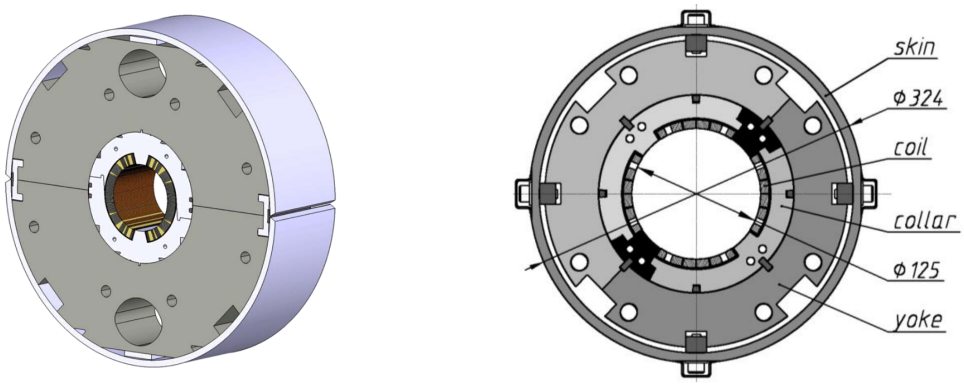

(a) (b)

Figure 14: (a) A slice of the 4.5 T SIS300 dipole magnet prototype [19]. (b) Cross section of the SIS300 quadrupole magnet prototype. [20]

The initial design of the FAIR facility required dipole magnets that could ramp from a field of 1.6 T to a field of 6 T at a rate of 1 T/s [21]. However, due to budget constraints the maximum field was reduced to 4.5 T [19]. In both designs, the magnets were designed to operate at 4.2 K and are of the $\cos(\theta)$ type. Both designs used NbTi superconducting Rutherford cables, with the 6 T design having 2-layers and the 4.5 T design, shown in Figure 14a, using a single layer. The coil aperture of the SIS300 dipoles is 100 mm.

A crucial element of the design of the SIS300 dipoles was the Rutherford cables used. During the ramp of a superconducting magnet, loss mechanisms, such as eddy currents, can create heat loads in the cables, which, if large enough can cause the magnet to quench [19]. The loss mechanisms can also cause the current in the cables to vary during the ramp, thus affecting field quality in the magnet. The Rutherford cables in the final design of the SIS300 dipoles were designed to reduce these losses. The cables were chosen to have 36, 0.825 mm wires arranged in two layers. Each wire had NbTi filaments surrounded by a copper stabiliser, with a copper to NbTi ratio, ν_{Cu-Sc}, of 1.5. A layer of 25 μm thick stainless steel tape was inserted between the two layers to reduce eddy currents between the layers. To reduce the eddy currents between wires in the same layer each wire was coated in a thin layer of tin-silver alloy.

To investigate the performance of the SIS300 dipole design, a full size prototype was built and tested [19]. In this preliminary test a ramp rate of 0.5 T/s was reached for a magnet swing of 2 T. The maximum ramp rate achieved was of 0.7 T/s, which was limited by the test cell used in this analysis. The central field value of 4.5 T was achieved when a current of 8926 A was passed through the coils. The peak field in the coils at this current was 4.9 T, resulting in a load margin of 69 %. AC losses in the cables were half as high as calculated losses and the field quality remained acceptable throughout the ramp.

As well as the dipoles, other magnets in SIS300 must ramp at a fast rate. In order to provide the same quadrupole focusing strength, k_1, the field gradient, g, of the quadrupole must increase with the increase in beam rigidity. Therefore, the quadrupole magnets must ramp at a rate proportional to the dipole ramp rate. To match the fast ramp rate of the dipoles the SIS300 quadrupole magnets must ramp from a field gradient of 16 T/m to a gradient of 45 T/m at a ramp rate of between 10 T/m/s and 20 T/m/s [20]. A prototype for the SIS300 quadrupole magnets has been produced, the design of which is shown in Figure 14b. The cables used for this design were similar to those used in the dipole designs, however, 19 wires were used, not 36 as in the dipole. The coil aperture for the quadrupoles is 125 mm, resulting in a pole tip field of 2.81 T. To reach this field a current of 6.26 kA was passed through the coils. The maximum field in the coils at this current was found to be 3.51 T. The critical current at 4.2 K and 3.51 T, is 9.3 kA, corresponding to a load margin of 48%. The field quality of the quadrupole was found to remain acceptable throughout the fast ramping cycle. The maximum ramp rate they were able to achieve was 36 T/m/s, far larger than the ramp rate required for operation.

3.1.5 Current Status of scSPS Magnets

Preliminary development of 6 T dipole magnets for the scSPS is underway [22, 23]. As shown in Figure 15, the design is based around existing LHC single aperture magnets, used in the final focusing system, and the SIS300 fast ramping magnets. The beam pipe aperture has radius 40 mm. As stated in Section 2, the optimal magnetic length is 12.12 m. Such a magnet would have a sagitta of 25 mm, therefore, to avoid making the aperture larger the dipole magnets will be curved. The coils are located at a radius of 45 mm, with 5 mm of radiation shielding between the coils and the beam pipe. The design has a single layer of 11 mm wide NbTi Rutherford cables based on the cables used in the SIS300 magnets and arranged in a $\cos(\theta)$ distribution. Each cable, therefore, has 26 individual wires arranged in two rows, with the same copper to NbTi ratio, ν_{Cu-Sc}, of 1.5. The operating temperature for the preliminary design is 1.9 K, thus requiring super fluid helium to provide cooling. The iron yoke surrounding the coils is laminated and has a radius of 228 mm. Detailed analysis have not yet been undertaken for this magnet design, but preliminary calculations have shown that to reach a central field of 6 T, a current of $\sim 11,000$ A must be passed through the coils. As yet, no work has been undertaken on the design of quadrupoles, sextupoles and octupoles for the scSPS.

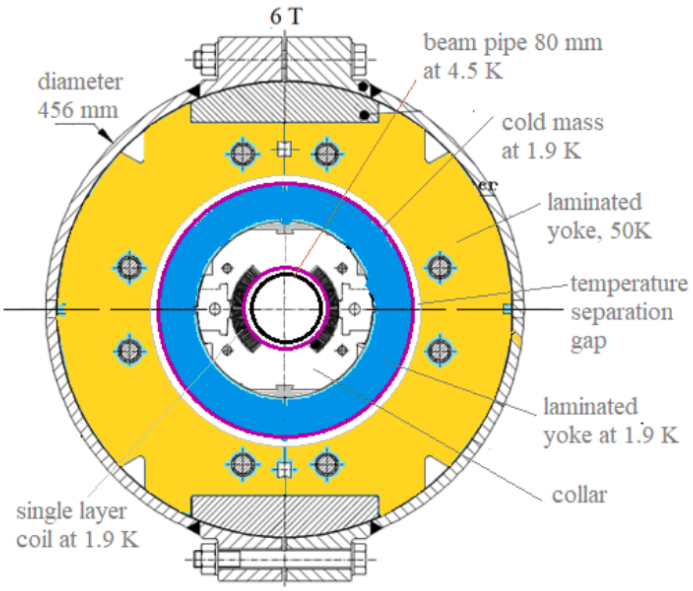

Figure 15: Preliminary scSPS dipole design, from [23].

3.1.6 Section Outline

During the course of our study, we were able to develop the preliminary designs for the scSPS dipole magnets. Quadrupole and sextupole magnet designs were also developed. The first subsection will discuss our designs for the superconducting dipole magnets, detailing three separate designs, one with a single layer of 11 mm Rutherford cables, one with a single layer of 15 mm cables and a 2-layered design. Next we shall discuss the designs for the scSPS quadrupole magnets, again 11 mm and 15 mm single layered designs and a 2-layered design. In the third subsection both superconducting and normal conducting designs for the scSPS sextupole magnets will be discussed. Finally, we will provide an insight into possible future work on magnet development.

3.2 Dipole Magnet Designs

3.2.1 Introduction

The SPS currently uses normal conducting magnets (see Fig. 16). These magnets are 6.3 m long with a magnetic field strength of 2 T, given that using a normal conducting design the maximum magnetic field that is typically achievable is 2 T, this is a key limitation of the SPS. The reason a normal conducting magnet cannot reach higher than 2 T is because the iron will saturate and the current required to increase the field by a substantial amount becomes unfeasible [24].

Figure 16: SPS Main Dipole Magnets in storage before installation [25].

To reach the desired extraction energy of 1.3 TeV the dipole magnets must ramp from 0.12 T to 6 T and be of a length of 12.12 m. Given this field strength a superconducting design is required, but there are many things to consider when designing a superconducting magnet, such as, the coil geometry, and the materials used. The dipole designs discussed here, all follow a $\cos\theta$ design, and use NbTi cables similar to those used in SIS300. As this is a preliminary study we did not model each individual cable, choosing to use the sector approximation to model each coil block. The iron yoke was not modelled with the holes that would be necessary to provide cooling to the magnet. For each magnet design the iron yoke was assumed to have the same outer radius as the preliminary dipole magnet design outlined in [23], 228 mm. To reduce the number of allowed magnetic field

harmonics each dipole was designed to have 2-fold symmetry. Each design was modelled using the finite element analysis software OPERA-2D [26].

3.2.2 11 mm Cables

The first dipole magnet design explored here uses 11 mm thick cables. In order to achieve a $\cos(\theta)$ distribution the magnet coils must follow a similar distribution, except, these are placed in discrete sets of coils. For this design, four sectors are used emulating four sets of coils. In order to achieve the $\cos(\theta)$ distribution there must of course be more coils in the sectors closer to 0° and less at 90°. This coil geometry is then mirrored and rotated for the other three quarters of the design, this suppresses even harmonics, and also makes the design simpler. Figure 17 shows one quarter of the design, starting from the smallest sector to the largest, the coils contained in each sector are; 2, 5, 9, 12 respectively. The spacing of the coil sectors is then dictated by the $\cos(\theta)$ field distribution.

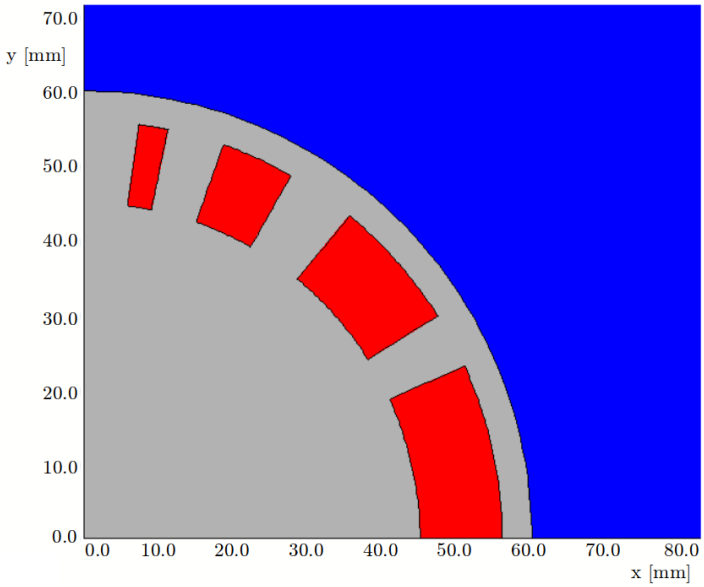

Figure 17: Cross section of 1/4 of a scSPS dipole magnet design with a single layer of 11 mm wide cables, shown in red. The iron yoke is shown in blue. Grey is used to represent a region containing no magnetic material.

Figure 18 shows the distribution flux density of the magnet coils in the 11 mm design. While the central field of the dipole is required to be a maximum of 6 T, in order to produce this, the flux density in the coils is required to be higher, this is important when considering operating currents, and also when evaluating how likely the magnet is to quench. Figure 18 clearly shows that the peak flux density is exhibited by the sector with only two coils at the top of the magnet.

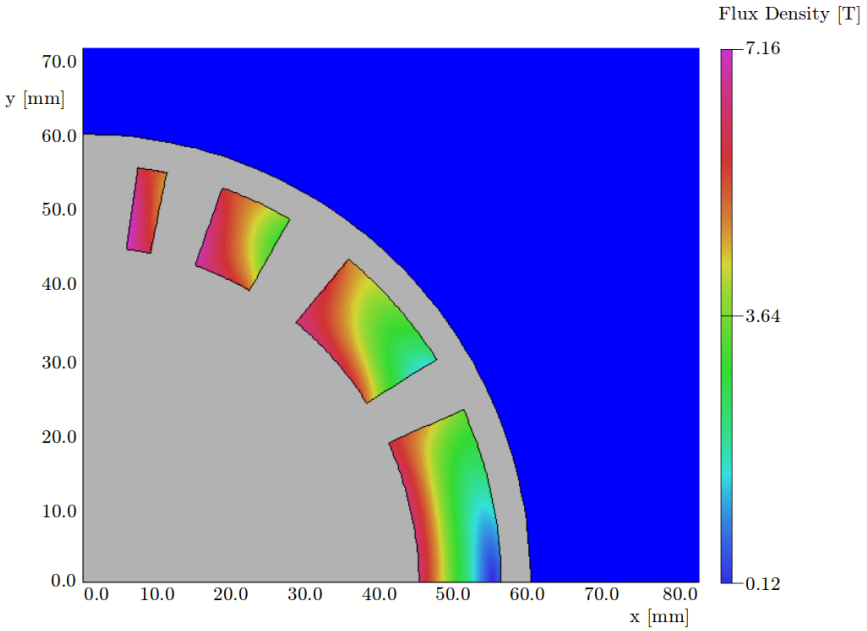

Figure 18: The distribution of flux density within the coils of the single layered dipole design with 11 mm wide cables.

To fully analyse this magnet design the magnet operating currents must be known, these currents have to ramp such that the magnet produces a central field, from 0.12 T at injection, all the way to 6 T at extraction. As such, a simulation was ran on this design to gather the current ramp. This design was shown to require an injection current of 214 A and an extraction current of 12 119 A. These values can then be used to check the field quality of the design. A good field quality is needed to ensure that the desired field is felt by all of the particles in the beam, as such, this should be as flat as possible. Table 5 shows the harmonics for the 11 mm design. These are reasonably low, but the b_3 harmonic is still a concern. It is thought that was some extra modifications, such as slightly shifting the coils, this could be reduced.

		I = 214 A	**I = 12,119 A**
$\mathbf{b}_1$	$[10^{-4}]$	10,000	10,000
$\mathbf{b}_2$	$[10^{-4}]$	-178.84	-40.68
$\mathbf{b}_5$	$[10^{-4}]$	82.07	90.16
$\mathbf{b}_7$	$[10^{-4}]$	4.17	5.57
$\mathbf{b}_9$	$[10^{-4}]$	6.09	6.68
$\mathbf{b}_{11}$	$[10^{-4}]$	-0.46	-0.49

Table 5: The normalised magnetic field harmonics for the single layered dipole with 11 mm wide cables, measured at the boundary of the good field region, 2/3 of magnetic aperture.

A key design parameter of a superconducting magnet is the cryogenics, while this report does not go into the design of the cryogenic system, it does look into what cooling agent will be needed. For these magnets the choice is between liquid helium at 4.2 K or super fluid helium at 1.9 K. Figure 19 shows the load lines for this design. Effectively this shows if the design can be operated at 1.9 K or 4.2 K. The working point of the design (shown by the +) shows the required current needed to obtain the necessary peak field that will produce the desired central field. As this is passed the critical current line for the 4.2 K, it can only be operated at 1.9 K, and with a load margin of 84%.

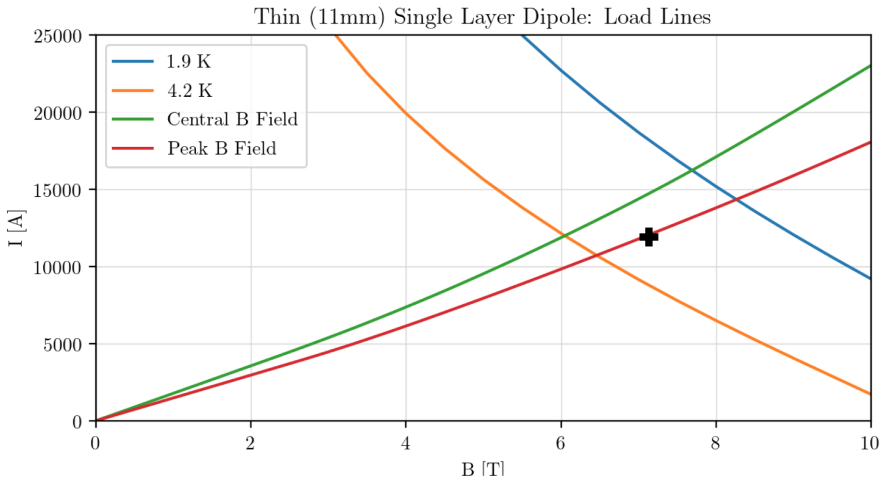

Figure 19: Load Lines for 11 mm Dipole Design

Overall this design should work, it produces the necessary field strengths with reasonable quality. It would have to be operated at 1.9 K, but at this temperature the load margin is reasonable. The design however could be improved with regards to field quality and in doing so would enable a cost effective design that has thin superconducting cables.

3.2.3 15 mm Cables

In an attempt to decrease the load margin over the 11 mm design the coils were thickened to 15 mm (see Fig. 20). This new design keeps the same coil geometry as before, of 2, 5, 9, 12. The peak B field required to deliver 6 T in the central field is slightly reduced from 7.16 T to 6.95 T, though the operating currents have now increased to 224 A for injection and 13 500 A for extraction.

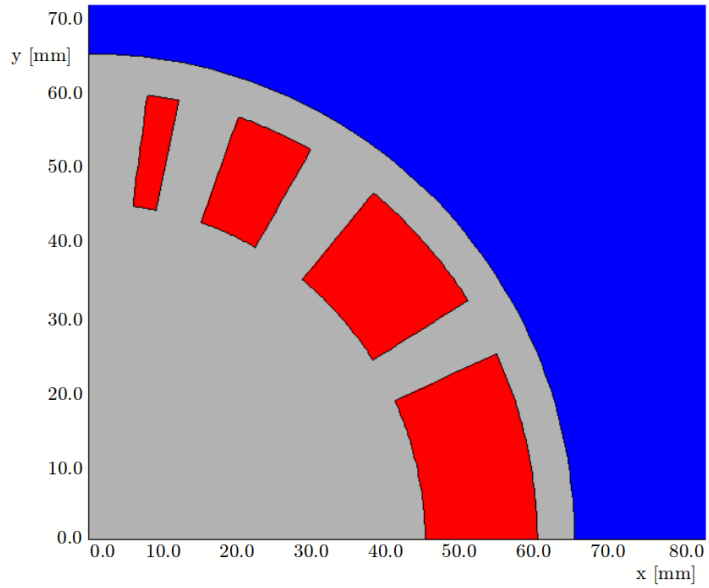

Figure 20: Cross section of 1/4 of a scSPS dipole magnet design with a single layer of 15 mm wide cables, shown in red. The iron yoke is shown in blue. Grey is used to represent a region containing no magnetic material.

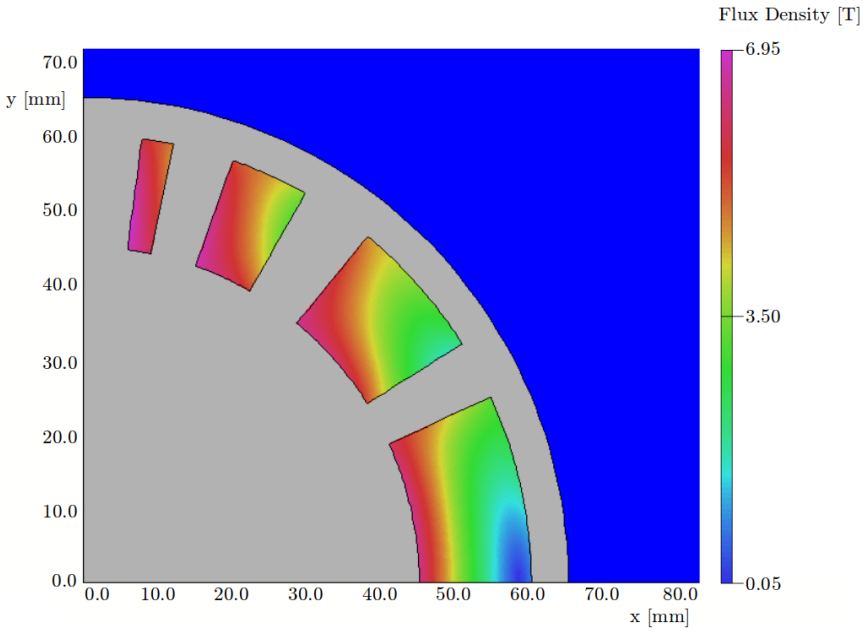

Figure 21: The distribution of flux density within the coils of the single layered dipole design with 15 mm wide cables.

		I = 224 A	**I = 13,500 A**
$\mathbf{b}_1$	$[10^{-4}]$	10,000	10,000
$\mathbf{b}_2$	$[10^{-4}]$	-138.50	-34.04
$\mathbf{b}_5$	$[10^{-4}]$	70.64	77.23
$\mathbf{b}_7$	$[10^{-4}]$	3.75	4.56
$\mathbf{b}_9$	$[10^{-4}]$	4.88	5.33
$\mathbf{b}_{11}$	$[10^{-4}]$	-0.39	-0.42

Table 6: The normalised magnetic field harmonics for the single layered dipole with 15 mm wide cables, measured at the boundary of the good field region, 2/3 of magnetic aperture.

These modifications result in a number of changes for the performance of the dipole. The harmonics of the design are all of the same order of magnitude, though they are slightly reduced (see Table. 6). The main improvement of this design is seen in Figure 22. This design allows the magnet to now be operated at 1.9 K with a load margin of 74%. While it no longer crosses the critical current line for 4.2 K, the margin is so tight that it is not feasible to run this design on liquid helium.

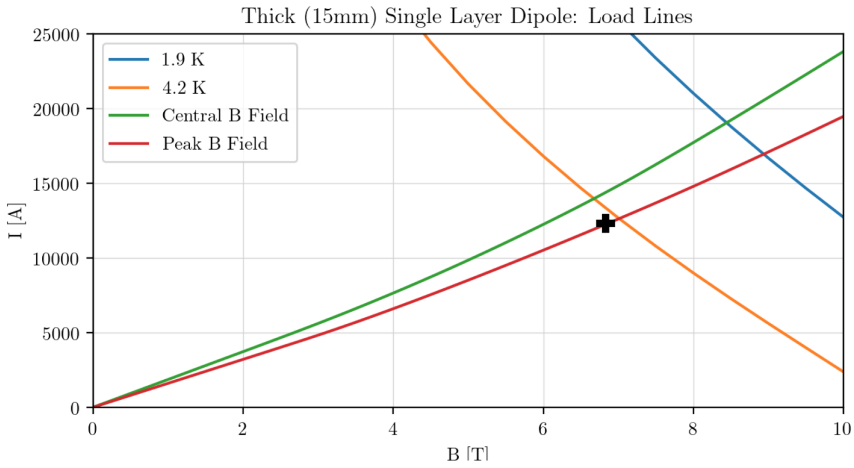

Figure 22: Load Lines for 15 mm Dipole Design

What this design shows is that by increasing the thickness of the coils the design becomes much more stable, both in terms of field quality and in terms of load margins. Once again, this design is a feasible dipole magnet that would fulfil the specification set, the harmonics could be reduced further with some slight geometrical changes, but this would be the only required change before taking this design to further steps.

3.2.4 2-Layer Design

In order to design a dipole magnet for the scSPS that could operate at at 4.2 K an additional layer of coils was added. Figure 23 shows this two layered design. The inner layer of this design has the same 2, 5, 9, 12 coil geometry of the 15 mm magnet design, whereas the outer layer has a block of 9 coils at 0° and 16 coils slightly above that. These outer layer coils are thinner at 11 mm, producing a grading between the two layers of 1.36.

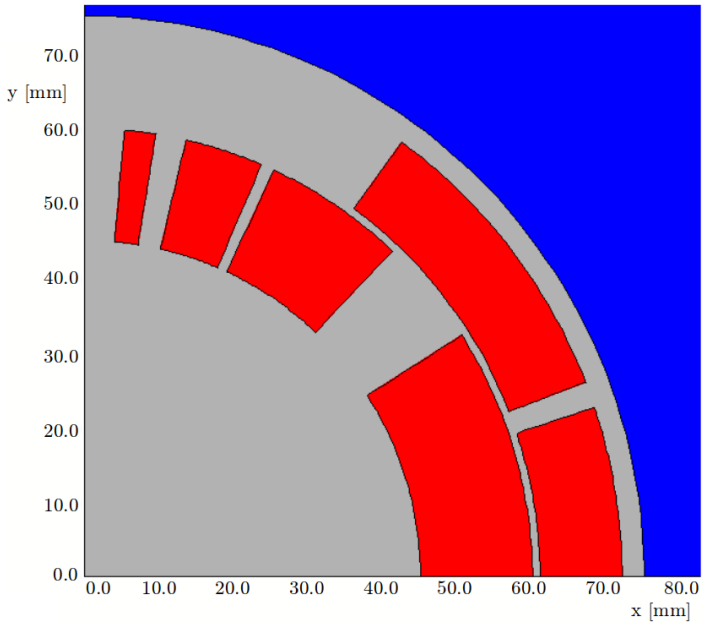

Figure 23: Cross section of 1/4 of a double layered scSPS dipole magnet design. The inner layer, 15 mm wide cables, and the outer layer, 11 mm wide cables, are shown in red. The iron yoke is shown in blue. Grey is used to represent a region containing no magnetic material.

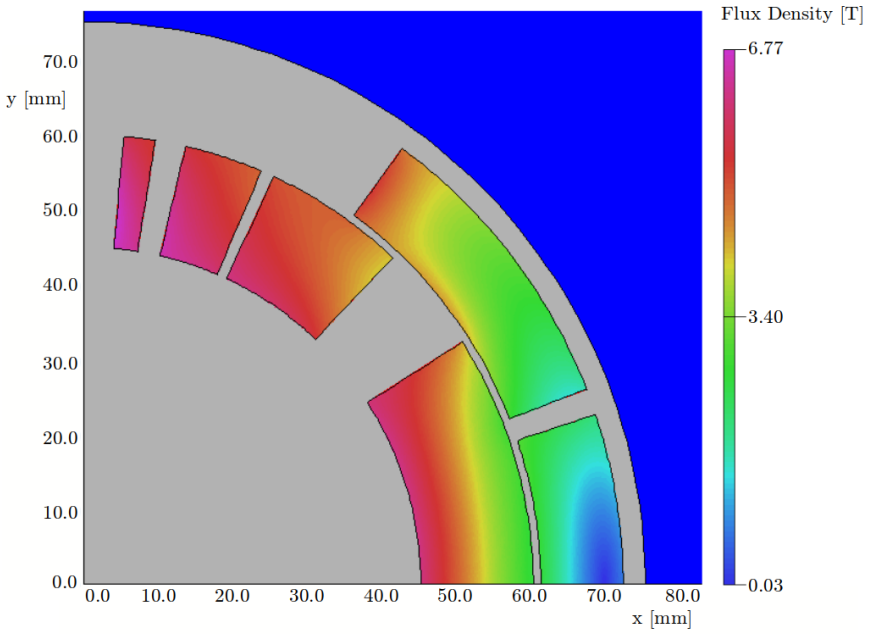

Figure 24: The distribution of flux density within the coils of the double layered dipole design.

By changing the coil geometry this way, the magnet performance is shifted. One key improvement is the harmonics. Table 7 clearly shows a reduction in the harmonics compared to the other two dipole designs, this creates a flatter field throughout the dipole aperture. The other key performance improvement is from the load lines. The second layer of coils allows the dipole to be ran at an extraction current of 6068 A. Figure 25 shows the load lines for the outer layer of the graded two layer dipole design. As the outer layer has tighter margins at 4.2 K and 1.9 K, only the outer layer is shown. As the operational current has now dropped, this magnet can now be operated using liquid helium as well as superfluid helium, in turn this gives the magnet an load margin of 84% at 4.2 K or an load margin of 62% at 1.9 K.

		I = 107 A	**I = 6,068 A**
$\mathbf{b}_1$	$[10^{-4}]$	10,000	10,000
$\mathbf{b}_2$	$[10^{-4}]$	-89.50	-57.85
$\mathbf{b}_5$	$[10^{-4}]$	64.93	75.56
$\mathbf{b}_7$	$[10^{-4}]$	-4.19	-4.90
$\mathbf{b}_9$	$[10^{-4}]$	-3.35	3.78
$\mathbf{b}_{11}$	$[10^{-4}]$	-0.49	-0.55

Table 7: The normalised magnetic field harmonics for the single layered quadrupole with 11 mm wide cables, measured at the boundary of the good field region, 2/3 of magnetic aperture.

Of the three magnet designs this one offers the most flexibility. It can be ran with two types of cryogenics, and has the largest load margins of all of the designs. This means that once manufactured, this design would be able to be upgraded in the future, by just changing the cryogenics, or the power supplies.

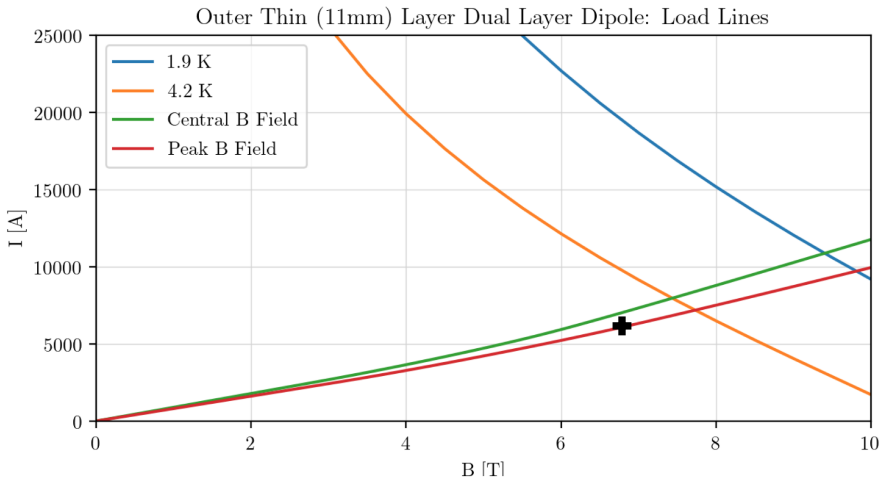

Figure 25: Load Lines for Graded Dipole Design

3.3 Quadrupole Magnet Design

3.3.1 Introduction

The quadrupole magnets for the scSPS must ramp from a field gradient of 2.82 T/m at injection to 146.25 T/m at extraction. As with the dipole magnets we produced three separate quadrupole magnet designs, one with a single layer of 11 mm thick Rutherford cables, one with a single layer of 15 mm thick Rutherford cables and a 2-layered design. Each design was of a $\cos(2\theta)$ type. Again we did not model each individual cable, choosing to use the sector approximation to model each coil block. For each magnet design the iron yoke was assumed to have the same outer radius as the preliminary dipole magnet design outlined in [23], 228 mm. As this is the first time scSPS quadrupole magnets have been designed, each yoke was not modelled with the holes that would be necessary to provide cooling to the magnet. To reduce the number of allowed magnetic field harmonics each quadrupole was designed to have 8-fold symmetry. Each design was again modelled using the finite element analysis software OPERA-2D [26].

3.3.2 11 mm Cables

Since the required central dipole field of 6 T could be achieved using a single layer of 11 mm wide Rutherford cables at 1.9 K, we used the same cables for our initial quadrupole design. The 11 mm quadrupole design is based on the design of the Q4 magnet used in the LHC interaction regions [3]. The cross section of one eighth of our design can be seen in Figure 26. Per eighth of the magnet cross section there are 14 coils split into three coil blocks. The largest block has 7 coils and is positioned on the horizontal axis, the second block has 5 coils and is centred at an angle of 22.2^o from the horizontal and the smallest block has 2 coils and is centred at an angle of 36.7^o from the horizontal.

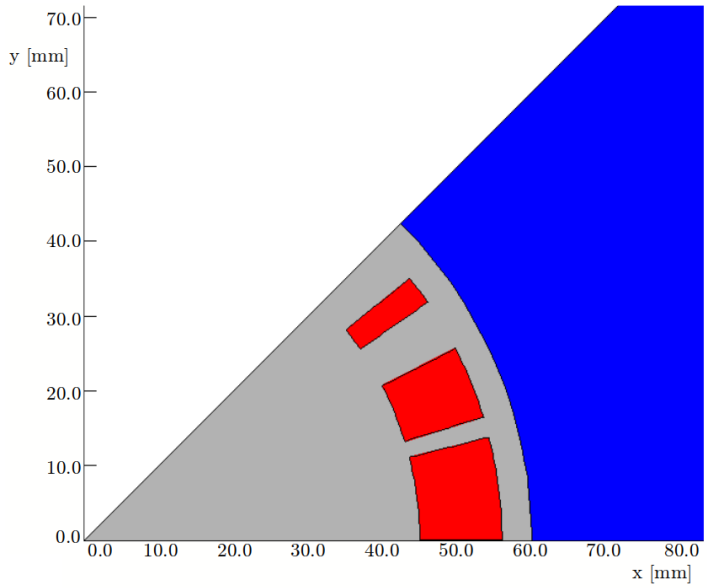

Figure 26: Cross section of 1/8 of a scSPS quadrupole magnet design with a single layer of 11 mm wide cables, shown in red. The iron yoke is shown in blue. Grey is used to represent a region containing no magnetic material.

The current needed at injection, was found to be 276 A, whilst the current required for extraction energies is 15697 A. As can be seen in Figure 27, the magnetic flux density was highest in the 2-coil block, which had a peak field of 7.27 T. The load line for the magnet is shown in Figure 28. From this it is clear to see that an operating temperature of 4.2 K is not possible. Although the operating point of the load line is lower than the critical curve for 1.9 K the magnet has a load margin of 95%, which is not acceptable for safe operation of an accelerator.

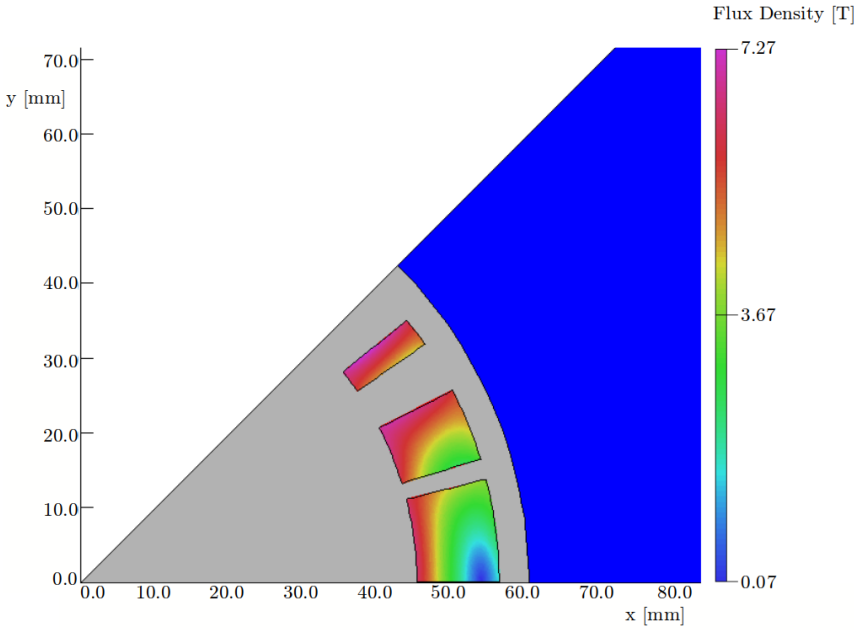

Figure 27: The distribution of flux density within the coils of the single layered quadrupole design with 11 mm wide cables.

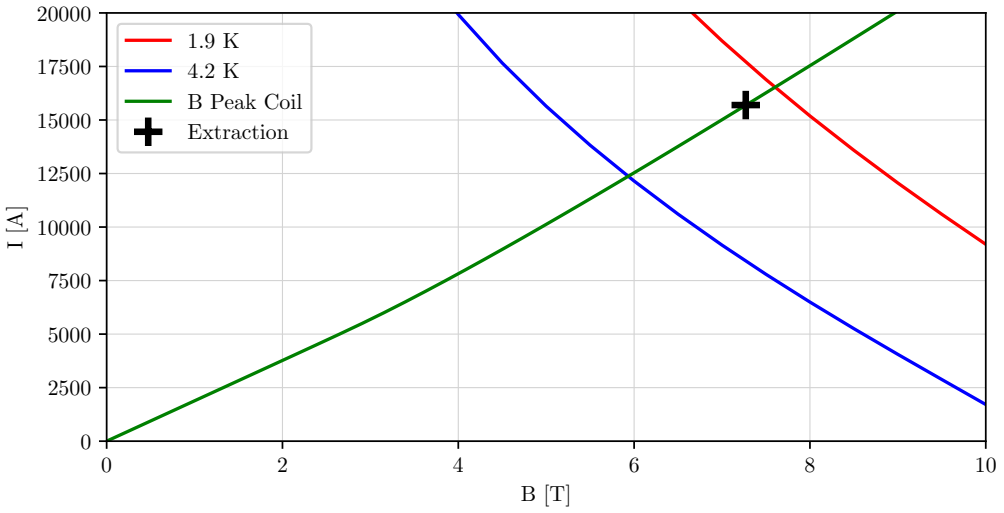

Figure 28: The load line for the single layer quadrupole design with 11 mm wide cables as well as the critical current-field curves for the 11 mm wide cables at 4.2 K and 1.9 K. The current and peak magnetic field at extraction is also shown.

The field quality, for this magnet design is good. The normalised field harmonics at 2/3 of the beam pipe aperture are shown in Table 8. These are within the acceptable limit for field quality of approximately 10^{-4} to a few 10^{-3} for both injection and extraction currents. The change in gradient over this region is also well within the acceptable limit, with a value of $\frac{\Delta g}{g}$ at injection of 3.12×10^{-3} and at extraction of 5.53×10^{-3}.

		I = 276 A	**I = 15,697 A**
$\mathbf{b}_2$	$[10^{-4}]$	10,000	10,000
$\mathbf{b}_6$	$[10^{-4}]$	-9.92	7.41
$\mathbf{b}_{10}$	$[10^{-4}]$	1.79	2.31
$\mathbf{b}_{14}$	$[10^{-4}]$	0.02	0.03
$\mathbf{b}_{18}$	$[10^{-4}]$	0.09	0.10

Table 8: The normalised magnetic field harmonics for the single layered quadrupole with 11 mm wide cables, measured at the boundary of the good field region, 2/3 of magnetic aperture.

3.3.3 15 mm Cables

Since the 11 mm design was shown not to be able to operate safely, the decision was made to use thicker cables. In this design, 15 mm cables with 36 wires were used. This would mean the current density would be lower in each cable, moving it away from the critical current density for NbTi. The coils were positioned at the same angles as in the 11 mm design with the inner radius of the iron yoke being made larger to accommodate the larger coils, Figure 29.

The current needed at extraction energy is 17,500 A with the current at injection equal to 305 A, both higher currents than the currents required for the 11 mm coils. However, the coil area for the 15 mm cables is 1.36 times larger than for the 11 mm cables, which results in a maximum current density in the 15 mm cables only 82% as high as in the 11 mm cables. As can be seen in Figure 30, the magnetic flux density was again focused in the 2-coil block, which had a peak field of 7.24 T, marginally lower than the 11 mm design. The load line for the magnet is shown in Figure 31. From this it is again clear to see that an operating temperature of 4.2 K is not possible. However, the operating point for the 15 mm design is significantly further from the load limit for the magnet at 1.9 K. The load margin for the 15 mm design is 86%. This value could be improved with small changes in the coil geometry, the yoke design or the cable design. With these small

changes this design could operate successfully in the scSPS.

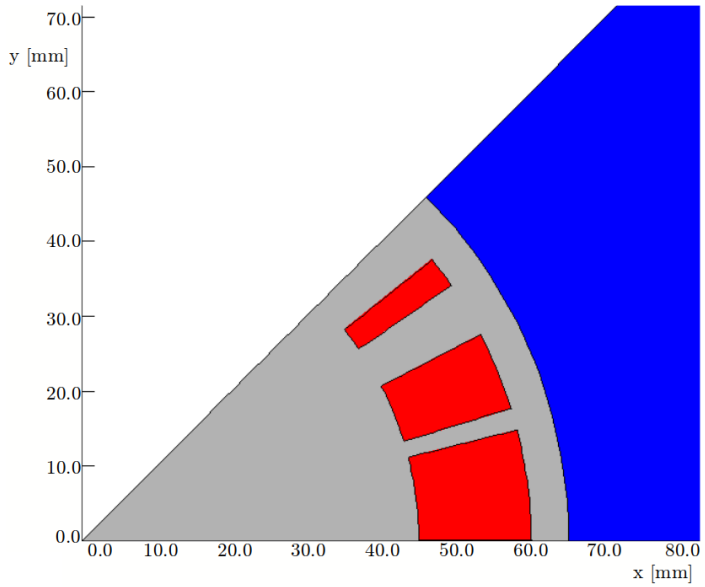

Figure 29: Cross section of 1/8 of a scSPS quadrupole magnet design with a single layer of 15 mm wide cables, shown in red. The iron yoke is shown in blue. Grey is used to represent a region containing no magnetic material.

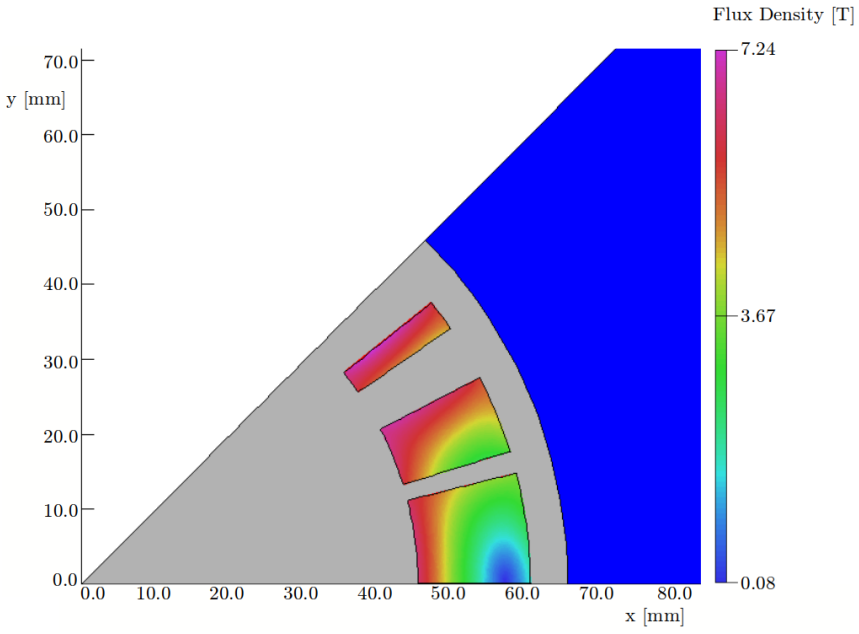

Figure 30: The distribution of flux density within the coils of the single layered quadrupole design with 15 mm wide cables.

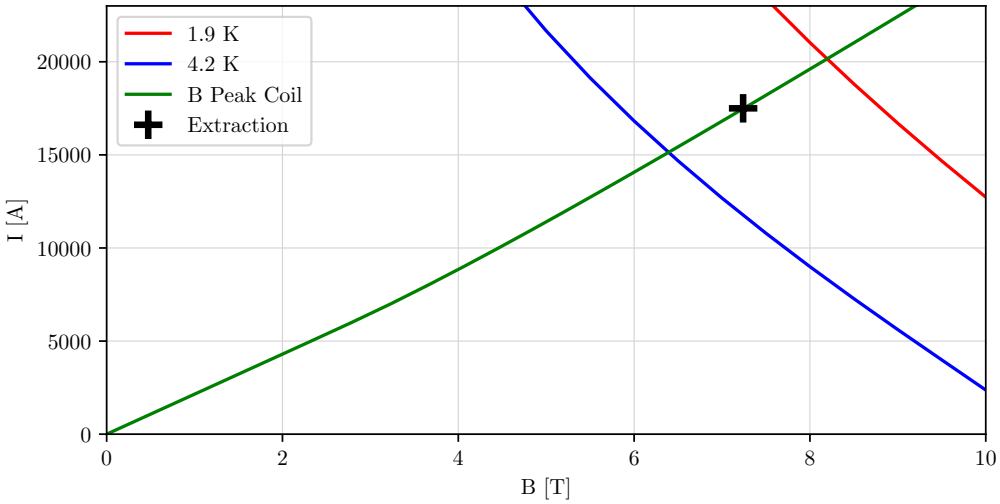

Figure 31: The load line for the single layer quadrupole design with 15 mm wide cables as well as the critical current-field curves for the 15 mm wide cables at 4.2 K and 1.9 K. The current and peak magnetic field at extraction is also shown.

The field quality, for this magnet design is similar to the 11 mm design. The normalised field harmonics at 2/3 of the beam pipe aperture are shown in Table 9. There are some small improvements in field quality, particularly at extraction current on the 11 mm design. These are again within the acceptable limit for field quality of approximately 10^{-4} to a few 10^{-3} for both injection and extraction currents. The change in gradient over this region is also well within the acceptable limit, with a value of $\frac{\Delta g}{g}$ at extraction of 2.83×10^{-3}.

		I = 305 A	**I = 17,500** A
$\mathbf{b}_2$	$[10^{-4}]$	10,000	10,000
$\mathbf{b}_6$	$[10^{-4}]$	-9.08	2.08
$\mathbf{b}_{10}$	$[10^{-4}]$	1.55	1.86
$\mathbf{b}_{14}$	$[10^{-4}]$	0.01	0.02
$\mathbf{b}_{18}$	$[10^{-4}]$	0.07	0.08

Table 9: The normalised magnetic field harmonics for the single layered quadrupole with 15 mm wide cables, measured at the boundary of the good field region, 2/3 of magnetic aperture.

3.3.4 2-Layer Design

Despite the 15 mm design showing that a single layer of NbTi Rutherford cables can be used for the scSPS quadrupole magnets, they cannot be used at a temperature of 4.2 K. To investigate whether operation at 4.2 K is possible for the scSPS we developed a 2-layer quadrupole design. As with the 2-layer dipole design the 2-layer quadrupole was designed with a grading of 1.36 between the inner cables, 15 mm wide, and the outer 11 mm cables. The geometry of the quadrupole magnet is based on the TQC01 magnet design, a Nb_3Sn single aperture magnet used in the final focusing system [27]. Figure 32 shows the geometry of one eight of the magnet design. Per one eighth, there are two inner blocks, each with 12 and 6 cables respectively, with a single outer block of 16 cables. The 12 and 16 coil blocks are both positioned to start at an angle of zero from the x axis. The position of the third block was varied to improve the field quality. The optimal angle was found to be 35.2^o from the x axis.

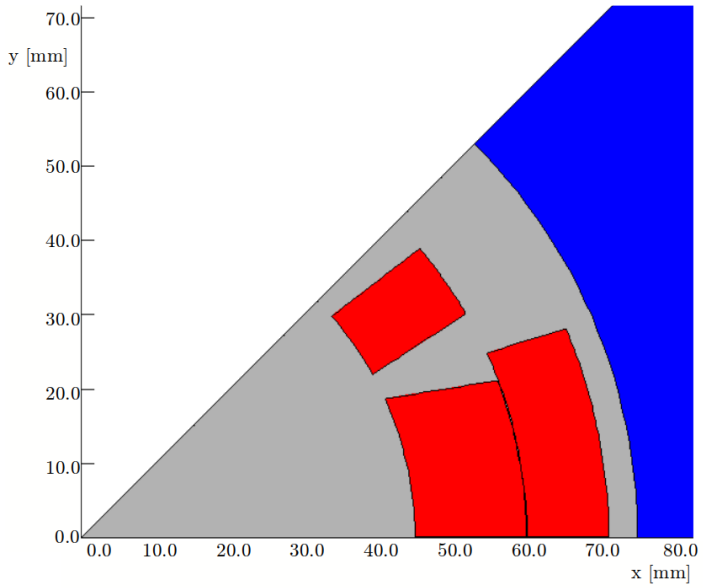

Figure 32: Cross section of 1/8 of a double layered scSPS quadrupole magnet design. The inner layer, 15 mm wide cables, and the outer layer, 11 mm wide cables, are shown in red. The iron yoke is shown in blue. Grey is used to represent a region containing no magnetic material.

The current needed at extraction energy is 8865 A with the current required at injection, 161 A. These are much lower than the currents required in the single layer design, with the current density being considerably lower. As can be seen in Figure 30, the magnetic flux density was focused on the smallest, inner, coil block, which had a peak field of 7.59 T. This magnetic field is higher than in any of the single layered designs, however, due to the current density being lower the operating point for the 2-layered design is significantly further from the load limit for the magnet at both 1.9 K and 4.2 K (Figure 34). The load margin at 1.9 K is 69 %, well within the safe region for reliable magnet operation. The load margin at 4.2 K, however, is 96%. This is too large for safe use, so changes to the magnet design must be made in order to operate at this temperature. One example of such a change would be to make the grading ratio larger than 1.36.

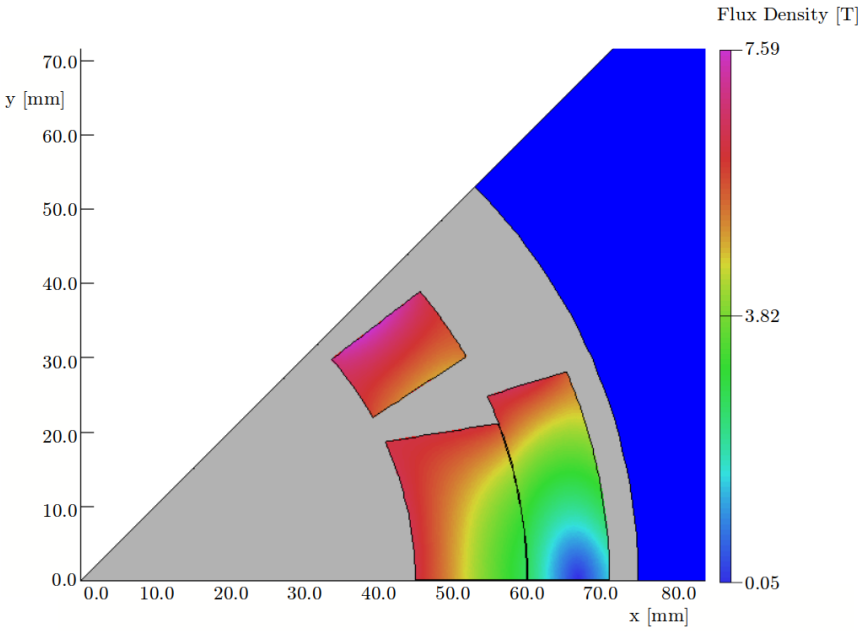

Figure 33: The distribution of flux density within the coils of the double layered quadrupole design.

The field quality, for the 2-layered design is again within acceptable limits. The normalised field harmonics at 2/3 of the beam pipe aperture are shown in Table 10. The field harmonics are slightly larger than for the single layered designs, which could be improved with small changes in the coil or yoke geometry. The change in gradient over this region is also well within the acceptable limit, with a value of $\frac{\Delta g}{g}$ at extraction of 1.44×10^{-3}.

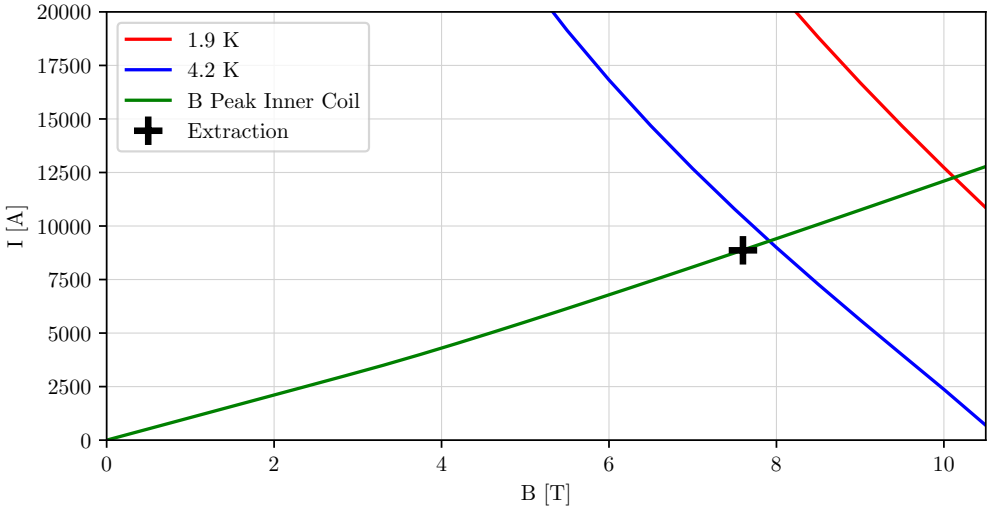

Figure 34: The load line for the inner layer of the 2-layered quadrupole magnet, current-field curves for the 15 mm wide cables, that are used in this inner layer, at 4.2 K and 1.9 K. The current and peak magnetic field at extraction is also shown.

		I = 161 A	I = 8865 A
$\mathbf{b}_2$	$[10^{-4}]$	10,000	10,000
$\mathbf{b}_6$	$[10^{-4}]$	-9.94	-8.67
$\mathbf{b}_{10}$	$[10^{-4}]$	5.28	5.95
$\mathbf{b}_{14}$	$[10^{-4}]$	-0.86	-0.96
$\mathbf{b}_{18}$	$[10^{-4}]$	0.04	0.04

Table 10: The normalised magnetic field harmonics for the double layered quadrupole measured at the boundary of the good field region, 2/3 of magnetic aperture.

3.4 Sextupole Magnet Design

3.4.1 Introduction

For the sextupole magnets, both resistive and superconducting designs were investigated. Since the peak field strengths required for the chromaticity correction are much lower than those required for the steering and focusing, it is possible to achieve the necessary field strength using resistive magnets. In these types of magnets the geometry of the iron pole has a dominant effect on the field quality, as opposed to superconducting designs where it is the wire geometry that dominates. In this section both types of magnets are considered.

Further to this, resistive cables can be split into two categories; air cooled and water cooled. Air cooled cables have the advantage of being cheaper and easier to implement than those requiring water cooling, but are limited to approximately 1.5 Amm^{-2}. In contrast, water cooled cables can reach current densities of 10 Amm^{-2}, and as such can significantly increase the pole tip field. An increased current density also increases the field in the iron, and as such the best yoke geometry will depend on the chosen current density.

As outlined in Section 2, a peak field of approximately 0.2 T is needed. However, due to the difference in placement of the sextupoles in the ring, the field requirements for the horizontal and vertical chromaticity correction differ, being 0.20 T and 0.33 T respectively. Designs for both these field strengths are presented. The design process involved first adjusting the current density and the wire area to meet the required field strength, and then modifying the yoke and wire geometry to improve the field quality. This process was carried out for air cooled, water cooled, and superconducting designs.

3.4.2 Air cooled magnet

Sextupole magnets exhibit twelve fold symmetry; each pole is mirrored about its axis and there are six identical poles. Figure 35 shows the segment for the air cooled magnet, capable of achieving a field of 0.2 T with a current density of 1 A mm^{-2}. Figure 36 shows the full sextupole magnet with contours showing the strength of the magnetic field in one of the poles. The peak magnetic field is found in the corner between the pole and the outer yoke, reaching a maximum value of 1.03 T, significantly below the 2 T limit beyond which the field cannot be appreciably increased. The angle between the pole and the outer yoke was chosen to be a right angle as this would make the magnets easier to manufacture, without pushing the field within the yoke beyond acceptable limits.

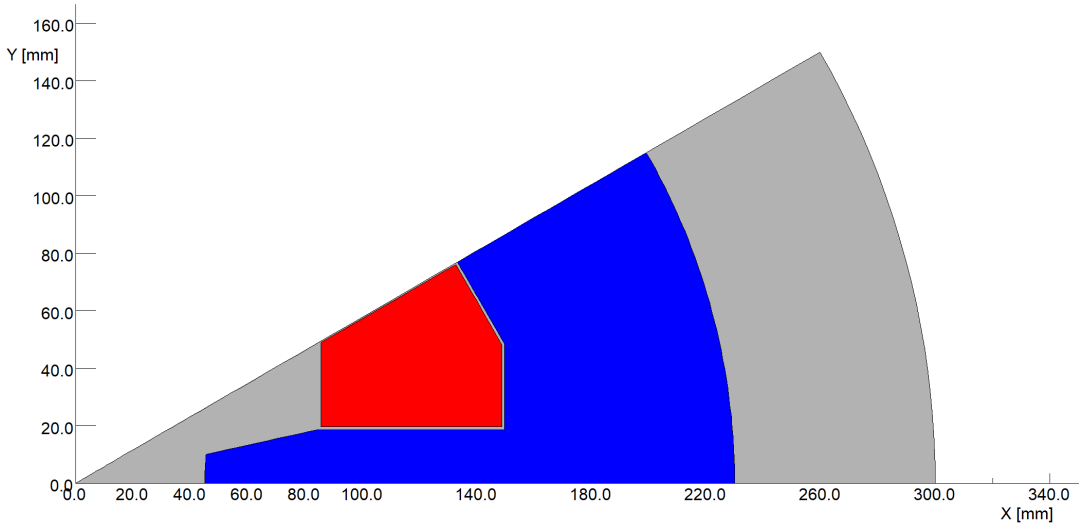

Figure 35: Segment of the air cooled sextupole.

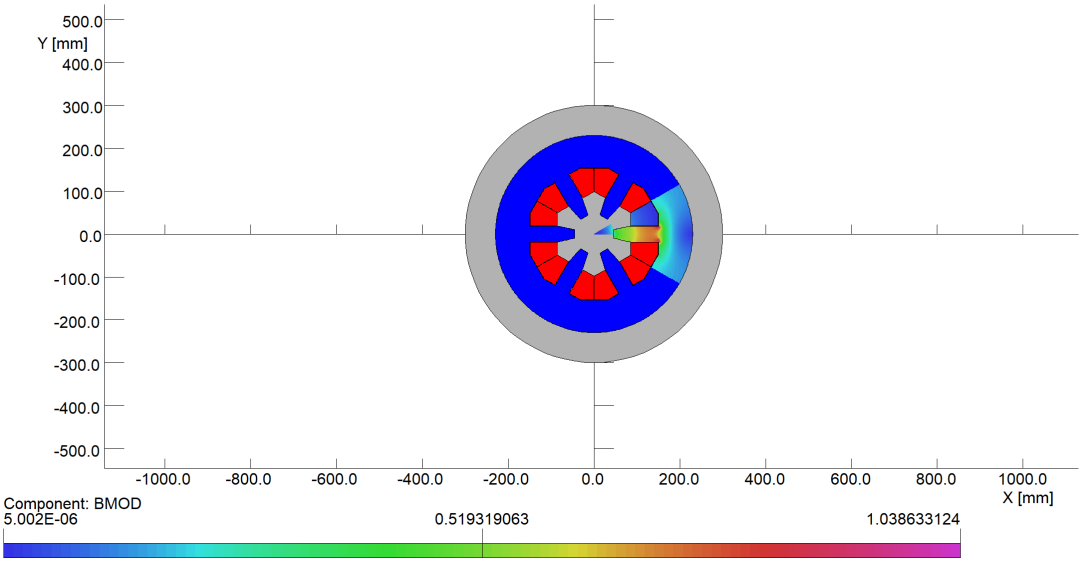

Figure 36: Full air cooled magnet.

3.4.3 Water cooled magnet

While the air cooled magnet is capable of achieving the 0.20 T field, the 0.33 T field requires a higher current. Since the area of the coil cannot be increased sufficiently without severely decreasing field quality, water cooled wires are required to increase the pole tip field. Figure 37 shows a segment of the water cooled design.

Since there is now a higher current, the yoke geometry requires modification to spread the field more evenly through the iron. The pole tip radius of curvature was increased to make the angle at the edge of the tip more oblique, and the thickness of the pole was increased to reduce the average field in the pole. These modifications reduce the area available for the coil, necessitating a current density of 3.2 Amm^{-2}. The peak field in the yoke reaches 1.8 T in the pole corners, which, while high, is still below the limit of 2 T. The distribution of the magnetic field in the pole can be seen in Figure 38.

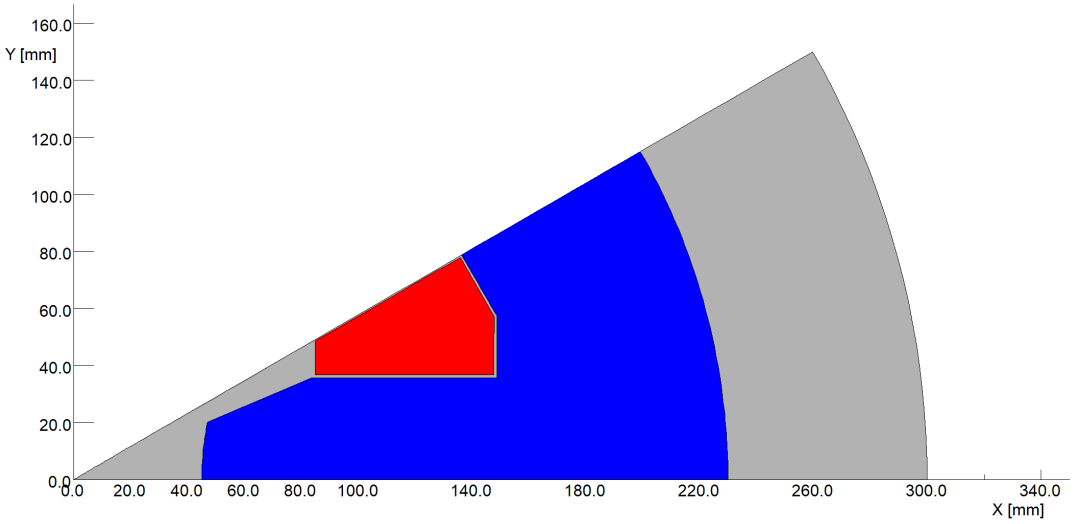

Figure 37: Segment of the water cooled sextupole.

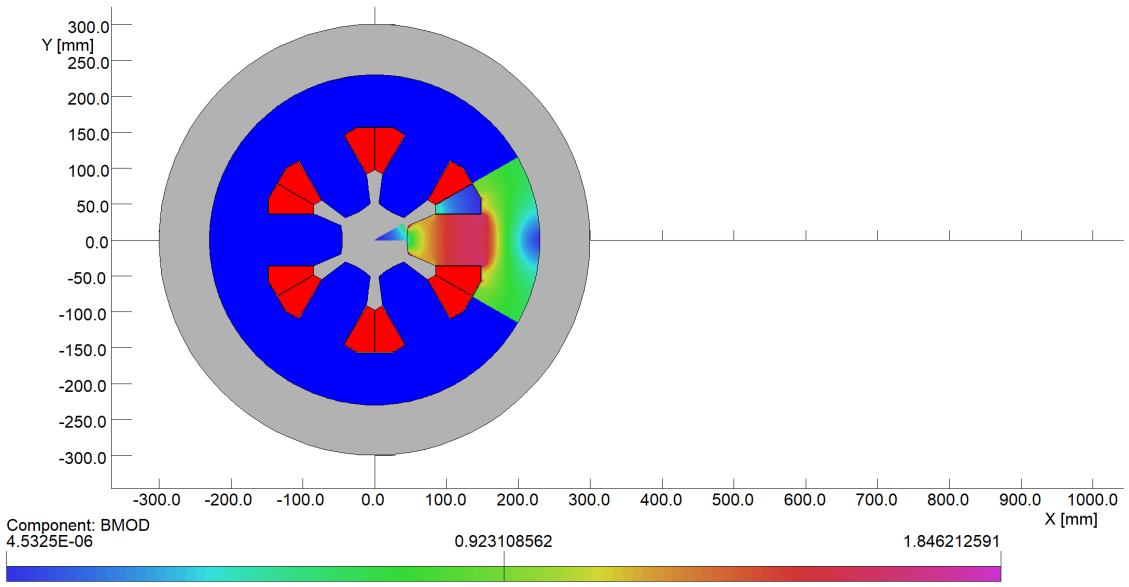

Figure 38: Full water cooled magnet

3.4.4 Superconducting magnet

Figures 39 and 40 show the segment design and field distribution for a superconducting sextupole with a peak field of 0.33 T. Here the current density is 40 Amm^{-2}, trivially attainable for a superconducting magnet. The design here uses a single layer coil with 11 mm cables, and this is all that would be necessary to achieve the required field strength with good field quality.

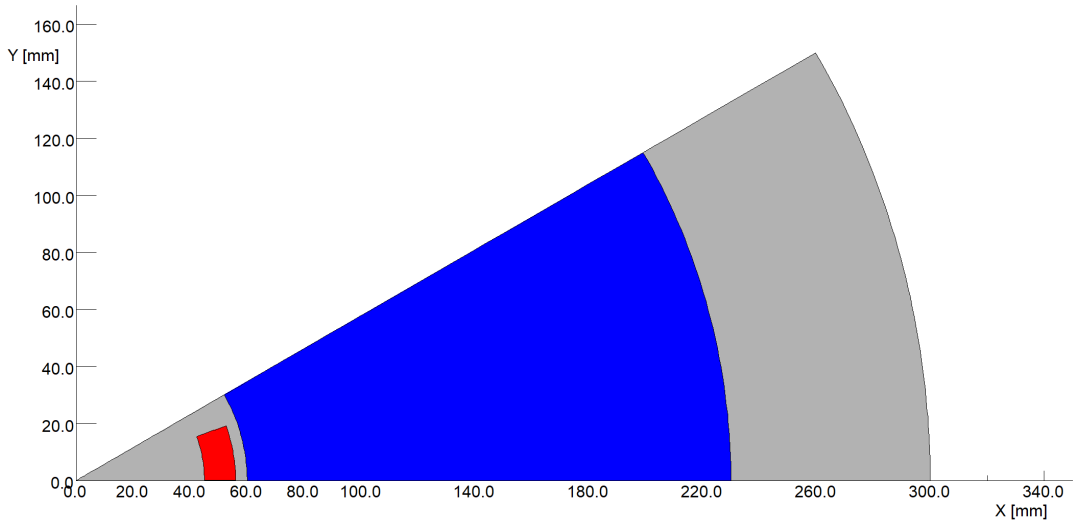

Figure 39: Segment of the superconducting sextupole.

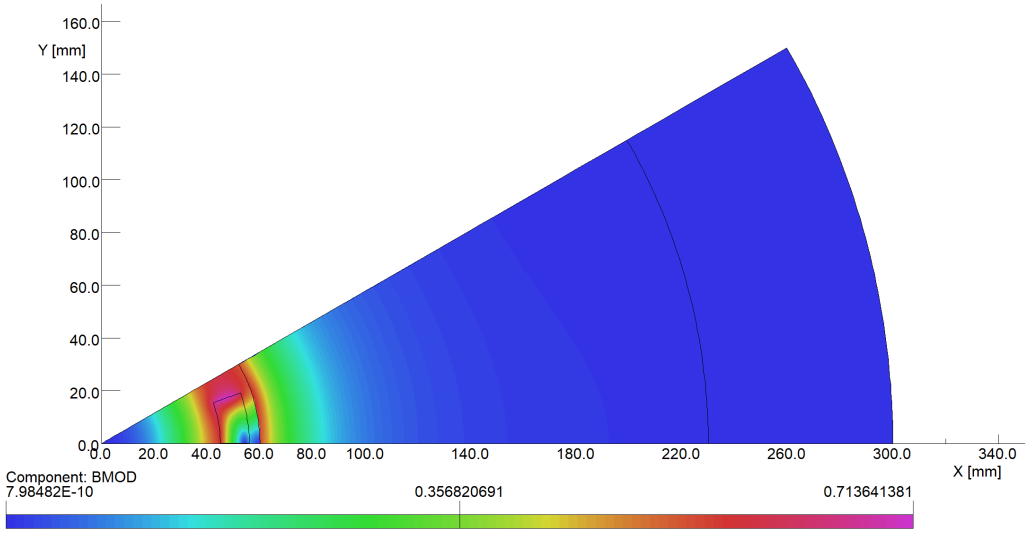

Figure 40: Field contours in a segment of the superconducting sextupole.

3.4.5 Field quality

Table 11 shows the harmonics for each of the three magnet designs shown. The field quality measurements are made at radius of 26.67 mm, and as can be seen, all coefficients are kept below the acceptable limit of 10^{-3}, indicating that these magnets would be suitable for use. A more rigorous optimisation of the magnet geometry could be performed to reduce these values further.

		Air cooled 1 Amm^{-2}	**Water cooled** 3.2 Amm^{-2}	**Superconducting** 40 Amm^{-2}
$\mathbf{b}_3$	$[10^{-4}]$	10,000	10,000	10,000
$\mathbf{b}_9$	$[10^{-4}]$	3.83	7.92	3.83
$\mathbf{b}_{15}$	$[10^{-4}]$	2.70	5.72	2.28
$\mathbf{b}_{21}$	$[10^{-4}]$	1.78	2.03	1.58
$\mathbf{b}_{27}$	$[10^{-4}]$	1.40	1.54	1.21

Table 11: Normalised magnetic field harmonics for the three sextupole magnet designs.

3.5 Outlook

Further optimisation of the magnets designed for this report could be undertaken. By altering the geometry of the magnets, the field quality and load margins could be increased, making the scSPS safer and more reliable, whilst providing a higher quality beam to the FCC-*hh*. By investigating AC losses around the injection field, we will be able to assess whether the current, 25 GeV, injection energy is viable. If not, it will be necessary to investigate injection from the PS2 at 50 GeV, with the costs associated with both injection options being assessed. All current work on magnet design has been done in 2D, 3D simulations must be done to fully understand the design, with care taken to the end of the magnets where the coils are turned around. The mechanical stresses must be evaluated for the magnets, particularly the superconducting ones where they will be very high. Doing this will allow for the design of the magnet collars. The thermal properties of the magnets must be evaluated. Specifically, the operating temperature of the superconducting magnets. The costs of extra cryogenic cooling to lower temperatures must be weighed up against the extra costs caused by having more cables at higher temperatures. Any improvements to field quality and AC losses at different operating temperatures must also be investigated.

4 RF Cavity

The RF system for any accelerator must be carefully designed to efficiently transfer power to the particle beam. In the case of synchrotrons, it is typical to place one RF system in the ring, which the particle bunch traverses once per turn, gaining energy each time. For the scSPS, the beam would be injected from the PS at 26 GeV with a 4.2 ns bunch length and extracted at 1.3 TeV into the FCC. The required cycle time is 30 s, defined by the requirements in filling the FCC-*hh* within $\simeq$ 30 minutes [2]. The energy swing required for the scSPS (50) is considerably greater than that of the current SPS (17) which extracts at 450 GeV. This factor is very important for the RF design as it will determine not only the voltage requirements, but also the range of RF frequencies which will be required to ensure the RF wave stays in phase with the particle beam on each revolution.

Synchrotron RF structures are tailored to each specific application, but the different options conventionally used are well illustrated by the current SPS and LHC cavities (see Figure 41a and 41b). The SPS uses normal-conducting cavities at 200 MHz which work in travelling wave mode. There are four such cavities in the ring, two of length 20 m and two 25 m, operating with 89 kV m^{-1} electric field [28]. The LHC on the other hand has superconducting cavities operating at 400 MHz. There are eight of these, each single cell, with a peak electric field of 5.3 MV m^{-1} [29], about 50 times greater than the SPS cavities.

(a) (b)

Figure 41: (a) SPS normal conducting cavities [28] (b) LHC superconducting cavities [30]

In this part of the report, the arguments for normal and superconducting cavities are presented for the case of the scSPS. Considerations for the frequency and voltage are explained and the difficulties specific to the large energy swing are considered in terms of the required frequency bandwidth. The shape and size of the structure is then varied to investigate the optimal parameters for acceleration using Poisson Superfish [31, 32] and CST Microwave studio [33]. The resulting design is described, with suggestions for future work. The design assumes the bunch supplied to the scSPS is the same as that received currently by the SPS, i.e. that the PS is not also upgraded for the FCC-hh injector. The advantages of upgrading the PS, to an extraction energy of 50 GeV and shorter bunch-length, are outlined.

4.1 Superconducting vs Normal Conducting Cavities

The major advantage of using a superconducting cavity, typically niobium, compared to a normal conducting cavity such as copper, is the great reduction in power loss due to surface resistance of the material. This makes superconducting cavities considerably more efficient, potentially by many orders of magnitude [34]. To quantify the reduction in power loss, we can consider the Q-value, defined;

$$Q = \frac{\omega U}{P_d} \tag{13}$$

where ω is the frequency of the cavity, U is the energy stored in the cavity and P_d is the power dissipated. For normal conducting cavities, it is common to find $Q = 10^5 - 10^6$, whereas for superconducting values of 10^{11} are easily reached. This directly translates to the RF power required for a given acceleration gradient, reducing thermal energy losses and cost.

However, when talking of power requirements it is also important to note that superconducting cavities require cryogenic cooling which is itself expensive and power consuming. Provided we are working with high energy beams, with low current and high duty factor, superconducting cavities are found to be the better option [34]. In the case of the scSPS, with up to 1.3 TeV protons, at 0.5 A [35] and duty factor close to 100 % [28], a superconducting cavity is the desired option for best efficiency.

The main disadvantages of a superconducting cavity are its increased cost and greatly reduced bandwidth. The cost comes in part from the construction of the cavity, but this can be minimised by instead of making the bulk structure out of superconducting material, use copper with niobium sputtering. The costs arising from the cryogenic system should be acceptable because the cryogenics will already be required for cooling of the dipole and quadrupole magnets. The small bandwidth of a superconducting cavity is a result of the high Q-factor, giving a low damping rate and long-lasting resonance. This causes problems for the scSPS design due to the large energy swing and hence non-negligible revolution frequency variation, which requires the RF frequency to vary over the cycle (see Section 4.4).

The other problems with using superconducting cavities are their inherent sensitivity to high electric and magnetic fields on the walls of the material, which could cause a breakdown of the superconductivity. The peak fields must be minimised during the design stage to ensure continued operation of the cavity (see Section 4.5.2).

It was decided that on the basis of the efficiency considerations, a superconducting design would be investigated for this project to determine whether such a cavity could be viable for the scSPS.

4.2 Voltage

The voltage for the RF cavity is determined by the energy increase required per turn. This corresponds directly to the ramping of the dipole magnets, whose bending field must increase to keep the more energetic beams on the correct orbit. This magnetic ramp rate is used to calculate the voltage with

$$V = \frac{2\pi R \rho \dot{B}}{T \sin \phi_s}, \tag{14}$$

where R is the average machine radius, ρ is the dipole bend radius, $\dot{B}$ the magnetic field ramp rate, T is the transit time factor and ϕ_s is the phase of the synchronous particle [36]. The maximum dipole ramp rate is $0.5\,\mathrm{T\,s^{-1}}$ and using the equation relating bending radius to magnetic field and beam energy, $B\rho\ [\mathrm{T\,m}] = 3.3356p\ [\mathrm{GeV}\,{c_0}^{-1}]$, and using the revolution frequency of 43.45 kHz, the maximum energy increase per turn is found to be 2.5 MeV.

The beam does not tend to be accelerated on the crest of the RF wave. This is because the beam has a non-zero bunch length and hence it is important to use the part of the wave that will cause a net focusing effect in longitudinal position. For our case, the synchronous phase is chosen to be $\phi_s \sim 120°$ during the acceleration. Considering also the fact that transit time factor is not equal to 1 but ~ 0.7, the peak voltage of the cavity is calculated to be 7.1 MV. For a single 75 cm cavity (see Section 4.5.2), this corresponds to a peak longitudinal electric field of $9.5\,\mathrm{MV\,m^{-1}}$, achievable with modern day superconducting technology. Multiple cells are therefore not required in this case. Effects of beam loading in such a cavity are calculated from theory to be small ($\sim kV$) and hence should not have much of an effect on the field amplitude [37]. For contingency, a value of $12\,\mathrm{MV\,m^{-1}}$ is used for the rest of the study.

The bucket area at this voltage was checked to ensure the scSPS could accept the bunch from the PS with a longitudinal emittance at 2σ of 0.35 eV s. The bucket area is given by the equation [36];

$$A_B = 16\sqrt{\frac{\beta^2 EeV}{2\pi\omega_0^2 h\,|\eta|}}\, a_b(\phi_s) \tag{15}$$

where β is the relativistic β of the protons, E is their energy, V is the peak voltage across the cavity, ω_0 is the revolution frequency, h the harmonic number, η is the slippage factor and a_b is a factor that takes into account a non-zero synchronous phase. A synchronous phase of 120° and a voltage of 12 MV m^{-1} gives $A_B = 340$ eV s at injection, thus easily containing the bunch.

If the scSPS cavity design opted instead for lower electric field structure, a multiple-cell cavity could be used instead, with other parameters the same. The single cell option, being cheaper and suffering less from bunch instabilities, is investigated in this report.

4.3 RF Frequency

The PS supplies bunches of 4.2 ns in bunch duration and so for maximum transfer efficiency, the RF waveform at injection must be able to capture the entirety of this bunch. This constrains the RF period to be longer than 4.2 ns, corresponding to an upper limit of 240 MHz for the RF frequency. This is low compared to the frequencies typically used in superconducting cavities, 300 to 1300 MHz [38]. The 200 MHz cavity of the current SPS can achieve reasonable transfer efficiency, and hence the frequency for the scSPS is chosen to have a similar value.

To satisfy the synchronicity condition with the bunches, the RF frequency must be an exact multiple of the revolution frequency $f_0 = \beta c/C$ where at extraction $\beta = 0.9999997$ and the circumference of the ring $C = 6.9$ km, giving $f_0 = 43.45$ kHz. Thus, the harmonic number is fixed at $h = f_{RF}/f_0 = 4605$ with $f_{RF} = 200.09$ MHz.

This determines the bucket structure within the scSPS. With 640 bunches required per cycle to fill the FCC-hh, at 25 ns spacing, there should be a bunch in every fifth bucket, leaving 7 µs of unfilled buckets which act as abort gaps (Figure 42).

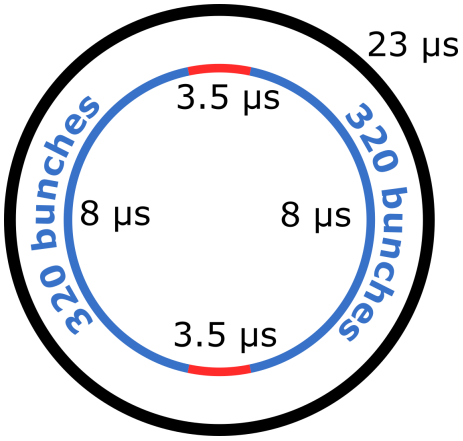

Figure 42: Bunch structure within the scSPS during each 23 µs turn, showing regions of bunches and abort gaps

Because the cavity works in standing wave mode, the RF frequency directly affects the required internal diameter of the cavity (see Figure 45). To get an idea of the dimension required, we can use the simple equation for a pill-box shaped cavity. For the transverse field to go to zero on the edge of the pill-box at 200 MHz, we require a 1.5 m diameter. This is large compared to conventional superconducting cavities, especially considering requirements for surrounding cryogenic equipment. The SPS tunnel has a radius of 2 m and hence the 200 MHz cavity should fit. If this is not sufficient space, there is also the possibility of using the old UA1 or UA2 caverns to house the RF cavity.

Although superconducting RF cavities at 200 MHz are not common, a prototype has been constructed and is shown in Figure 43 to give an idea of what is possible [39] [40]. This is a copper design with niobium sputtering, thus optimising the cost. Although designed for a muon accelerator, the cavity matches well to the requirements of the scSPS, with a peak field achieved of 11 MV m^{-1} [40].

It may be worth considering the option of having two different cavities, one at 200 MHz to catch the 4.2 ns beam from the PS and one at 400 MHz to accelerate the beam once its bunch

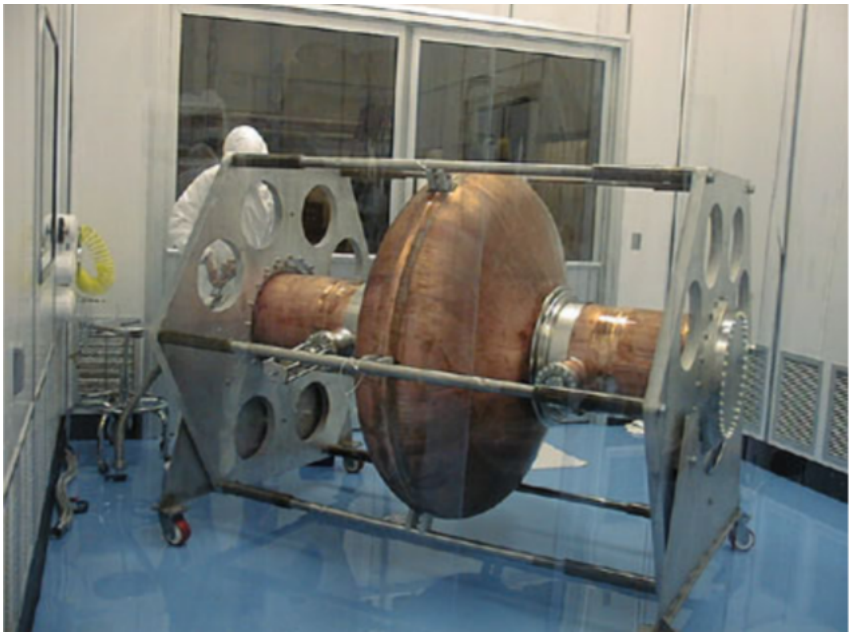

Figure 43: 200MHz superconducting cavity prototype
[40]

length had decreased sufficiently. The 200 MHz cavity could be very similar to the current SPS normal conducting cavity and hence reduce the requirements on the design of a superconducting cavity at such a low frequency. This scheme would however introduce additional complications in transferring from one system to the other. For this project, it was decided to design a 200 MHz superconducting cavity to explore what would be possible with such a cavity and whether it could be a viable option for the scSPS.

4.4 Tuning

The scSPS is currently being proposed with an injection energy of 26 GeV from the PS to extraction into the FCC-hh at 1.3 TeV. This change in energy has a non-negligible effect on the revolution frequency of the protons, and hence on the RF frequency. With a 200 MHz RF system, the RF bandwidth required is 130 kHz, as can be seen in Figure 44a. The natural bandwidth of a superconducting cavity can be calculated using the simple expression $Q = \omega/\Delta\omega$. For $Q = 10^{11}$ and $\omega = 200\,\text{MHz}$, it is found that $\Delta\omega = 2 \times 10^{-3}\,\text{Hz}$, six orders of magnitude too small to compensate for the changing energy of the beam.

Therefore, it will be important for external tuning systems to be used to achieve the RF frequency change from injection to extraction. Broadly speaking, RF cavity tuners come in two types: fast tuners, for example using piezo-electric technology, with a bandwidth of $\sim 5\,\text{kHz}$, and slow tuners, using stepper motors, with a bandwidth of $\sim 250\,\text{kHz}$ [41]. Figure 44b shows how the tuning rate required for the scSPS varies during the 34 s cycle. It is clear, that just after injection, the rate of increase of frequency required to keep up with the beam is at a maximum of $370\,\text{kHz}\,\text{s}^{-1}$. This is in the realm of fast tuners. However, the required bandwidth of 130 kHz is not achievable by the traditional piezo-electric tuners.

Discussions with experts suggest that a tuner meeting the requirements of the scSPS cavity could be possible. There already exists a tuner which appears to satisfy the requirements [42], with a variation of 200 kHz achieved in a matter of milliseconds. Within the time frame of the commissioning of the full FCC-hh project, it is hoped that a tuner which exactly fits the scSPS specification could be designed and commissioned.

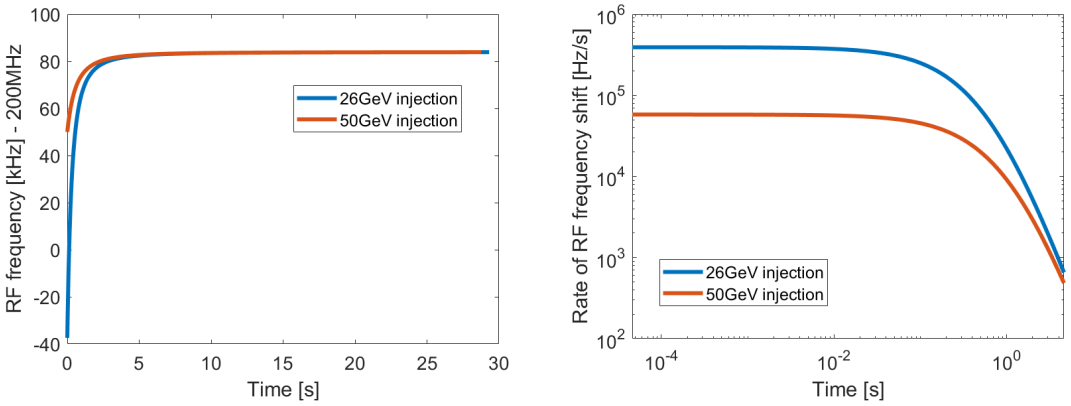

(a) (b)

Figure 44: (a) RF frequency required as a function of time during the cycle to stay in phase with the synchronous particle. (b) Rate of frequency change required as a function of time during the cycle

4.5 Design Considerations

Multi impacting, or "multipacting" is a process whereby electrons emitted from the cavity surface gain energy in one period of the electromagnetic field and return to their and collide with the surface. If a resonant condition is satisfied and provided the secondary electron emission coefficient is > 1 this can lead to electron multiplication. If sufficient energy is deposited into the cavity surface in this way, local heating can lead to a breakdown of superconductivity reducing the quality factor of a cavity. Overcoming this problem requires a detailed study of the cavity geometry using codes such as multipac [43] or CST [44]. While a detailed analysis will not be performed for this analysis, care will be taken to avoid a geometry which resembles pillbox with parallel faces as this would lead to severe multipacting issues [38].

Field emission is a process where the electric field at the surface of a cavity reduces the potential barrier which ordinarily prevents electrons from escaping the material [45]. Field emission occurs in the presence of high surface electric fields [46], and was partially responsible for the drop in quality factor of the prototype 200 MHz cavity [40]. To reduce the affect of field emission the peak surface field should be minimised, which, practically means reducing $E_{\text{peak}}/E_{\text{acc}}$ where E_{peak} is the peak electric field at the cavity surface and E_{acc} is the average accelerating field of the cavity.

The effects of multipacting and field emission must be considered whilst also reducing the impact of higher order modes (HOMs), and ensuring the surface magnetic field does not surpass the critical field of the superconductor. In addition to these primary concerns, both the shunt impedance ZT^2 and the quality factor should be kept relatively high so as to optimise ZT^2/Q. A large value of ZT^2/Q results in large transient beam loading and values of around $100\,\Omega$ have been used in previous cavity designs [47]. The basic geometry for a single-cell superconducting elliptical cavity is shown in Figure 45. The variable parameters include: b_D, $\frac{a_D}{b_D}$, α_w, $\frac{a_I}{b_I}$ and R_b, which must be optimised.

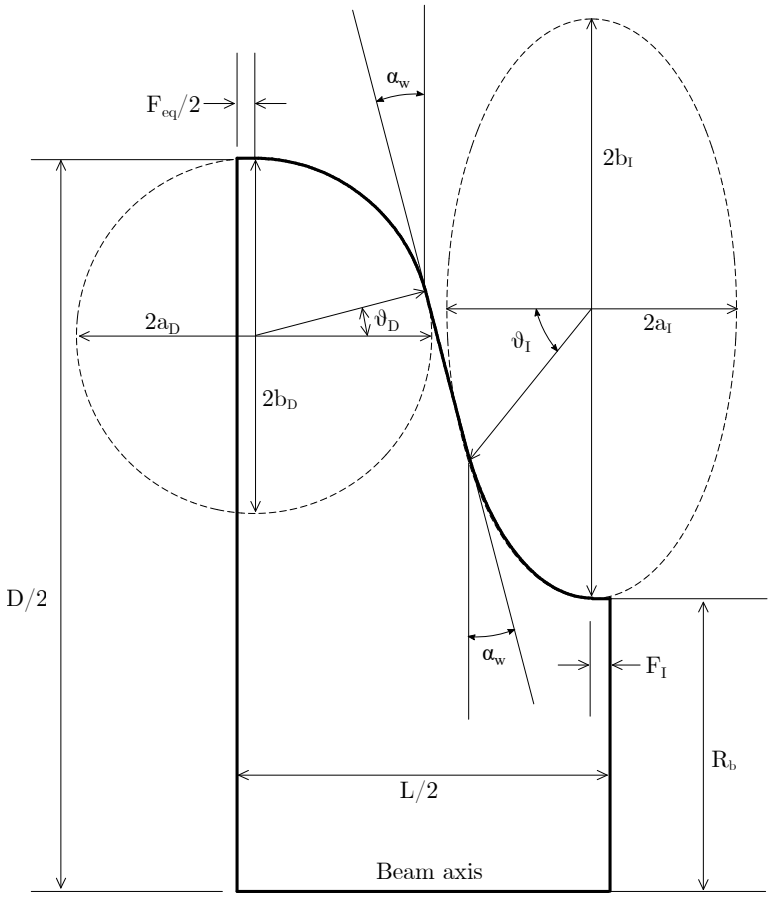

Figure 45: Geometry of an elliptical cavity.

4.5.1 Higher Order Modes

Solutions to Maxwell's wave equations within structures consisting of a single conductor contain an infinite series of electromagnetic modes. For a given mode to propagate inside a structure the frequency of the electromagnetic wave must exceed some cutoff frequency so that in practice the infinite series is truncated, in many practical cases after only one or two modes [48]. An example of such modes in an elliptical style cavity are shown in Figure 46. Individual modes are identified with three subscripts, m, n, l which describe the field distribution in a cylindrical waveguide cavity. Cavities of similar geometries, such as elliptical cavities, can have modes with similar field distributions. In particular the cylindrical TM_{010} mode, which is commonly used to accelerate particles, is often the lowest frequency mode in both cylindrical and elliptical cavities. The axial electric field and azimuthal H field of this mode make it particularly useful for accelerating particles (see Figures 46a and 46b). Modes with frequencies higher than this are often referred to as "higher order modes" (HOMs). These HOMs are responsible for large narrow-band beam coupling impedances and depending on the field distribution can result in either longitudinal or transverse beam instabilities.

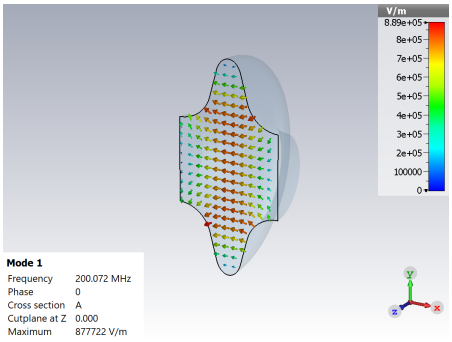

(a) Electric field of mode 1 at 200 MHz.

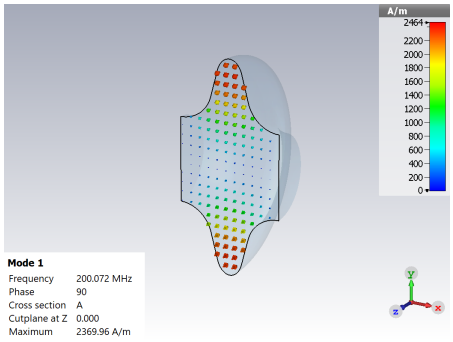

(b) H field of mode 1 at 200 MHz.

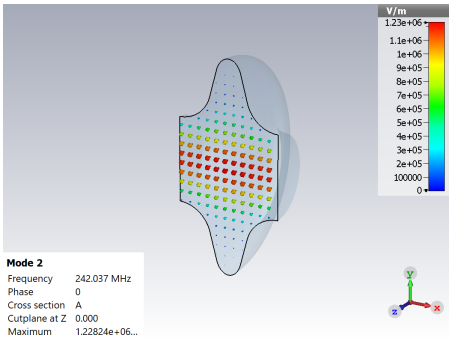

(c) Electric field of mode 2 at 242 MHz.

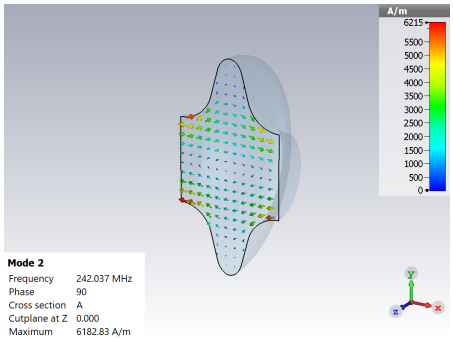

(d) H field of mode 2 at 242 MHz.

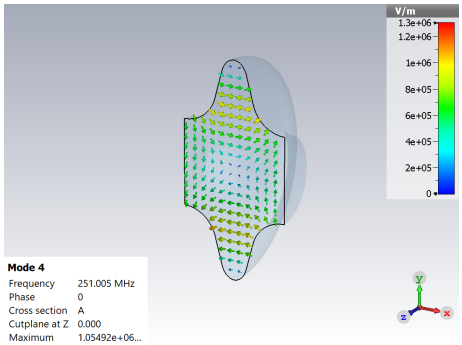

(e) Electric field of mode 4 at 251 MHz.

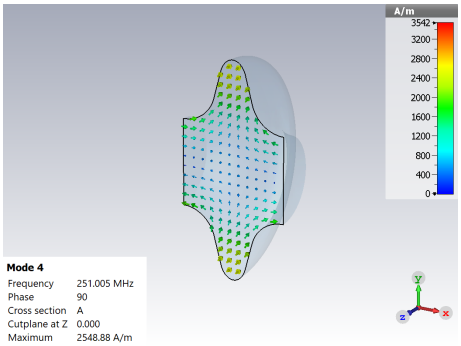

(f) H field of mode 4 at 251 MHz.

Figure 46: First few modes for a typical elliptical cavity geometry.

The RF power supplies which feed the cavity will operate at this frequency so that in the absence of other driving terms the cavity will resonate with only a TM_{010} mode. When a charged particle beam traverses the cavity, it too will excite modes but in this case the spectrum of the driving field is primarily determined by the longitudinal structure of the bunch. Injected bunches are expected to be approximately gaussian with a 4σ width of 4 ns [49], Figure 47a shows an approximate time structure for such a bunch and Figure 47b shows the associated spectrum for this bunch. The driving field spectrum extends to $\approx$1 GHz, so that modes with a cutoff frequency below this will be excited. At least the first four modes of the 200 MHz cavity in Figure 46 could be excited as they occur at frequencies below 1 GHz.

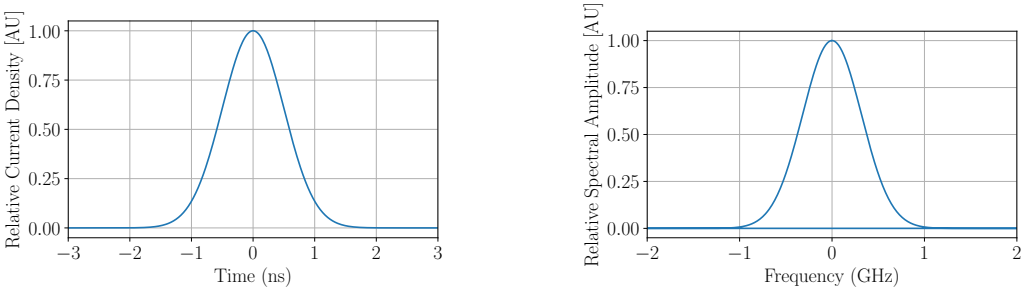

(a) (b)

Figure 47: Approximate (a) time structure of a PS bunch and (b) single bunch spectrum.

One method of suppressing HOMs is to increase the radius of the beam aperture so that the vacuum chamber acts as a waveguide. In the case of a cylindrical waveguide cavity this requires that the aperture radius, R_b is at least half the radius of the cavity R_c; assuming the first HOM is the TM110 mode, see Appendix 5. This approximate solution neglects the impact of the apertures on the HOM frequencies and in practice numerical solutions are required. Other practical considerations can limit the aperture radius, such as the potential for vacuum leaks at the end flanges [40]. In practice the aperture radius can only be maximised whilst satisfying these additional considerations. If higher order modes are expected then additional HOM couplers can be added [29].

A series of SUPERFISH simulations were run with varying aperture radii; the template ELLFISH input is listed in Appendix 5 and a subset of the resulting cavities are shown in Figure 48. For each bore radius setting the cavity radius was varied to produce a 200 MHz resonant frequency. A beam tube was included on the right hand side as the boundary condition applied by the simulation are not well satisfied with large beam apertures.

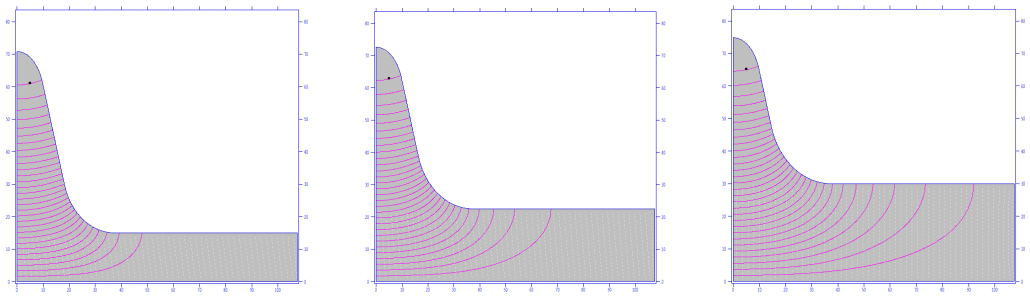

(a) (b) (c)

Figure 48: Geometry of SUPERFISH simulations with an aperture radius of (a) 15 cm, (b) 22.5 cm and (c) 30 cm.

Figure 49d shows that increasing the bore radius reduces the transit time factor. This is can be qualitatively understood from Figure 48 which shows the electric field contours extending further into the surrounding beam pipe. The transit-time factor cannot be arbitrarily small given a certain accelerating field and cavity length. Rearranging equation (14) gives

$$T > \frac{2\pi R \rho \dot{B}}{E_0 L \sin(\phi_s)}, \tag{16}$$

$$> 0.6 \tag{17}$$

where the properties listed in Table 2 have been used and it was assumed that $\sin(\phi_s) = 0.5$. The length was set to $L = \frac{\beta c}{2f} = \frac{\beta \lambda}{2} \approx 0.75\,\text{m}$. The maximum accelerating field was taken to be $11\,\text{MV}\,\text{m}^{-1}$; the maximum accelerating field achieved with the prototype muon cavity [40]. Figure 49d shows that a bore radius of 22 cm can satisfy this requirement with some contingency. In

addition choosing a larger aperture radius reduces the peak fields at the cavity surface as shown by Figures 49a and 49b.

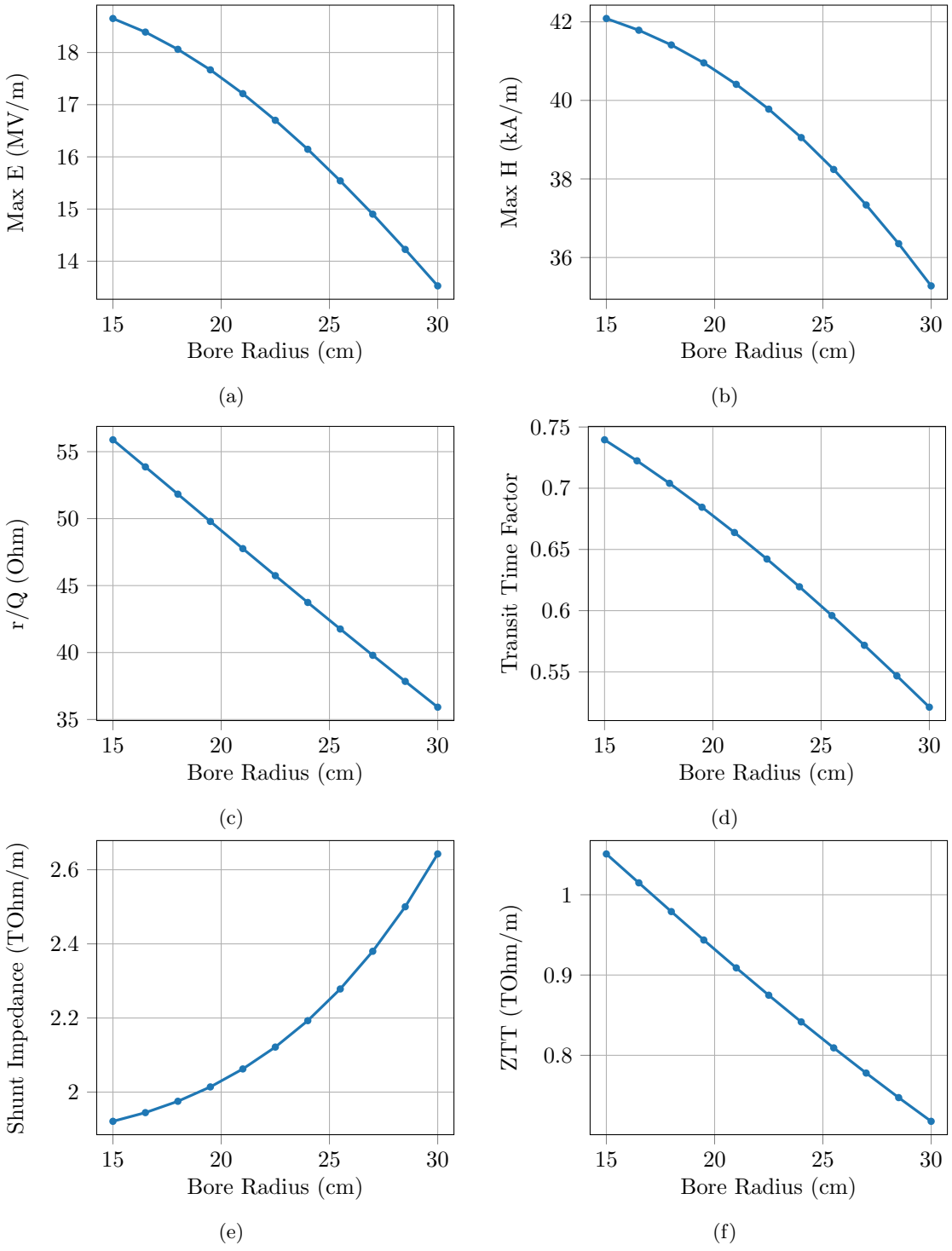

Figure 49: Results from half-cavity ELLFISH simulations where the bore radius was varied; note that r/Q is half of the full cavity value.

4.5.2 Surface Electric Field

To investigate the impact of surface electric field with the geometric parameters a series of SUPERFISH simulations were run for varying parameter values. For each of these sweeps a template

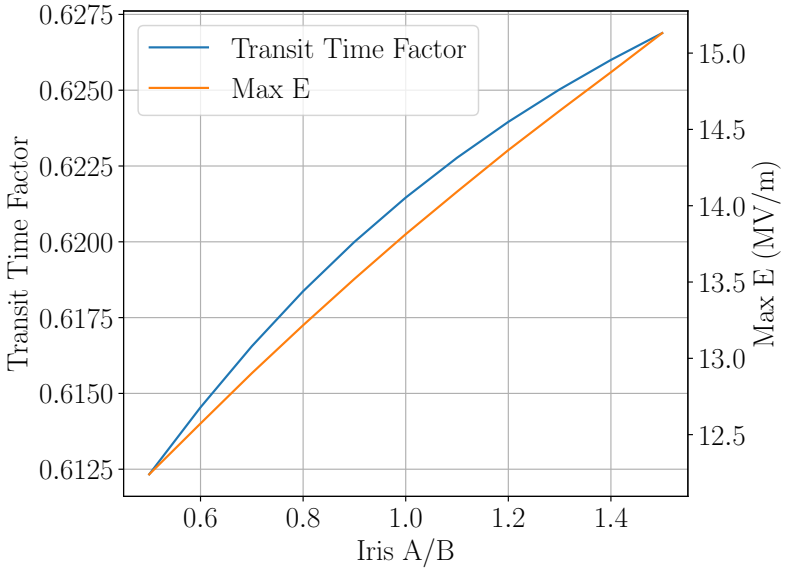

Figure 50: Transit time factor and peak surface electric field for a range of values for a_I/b_I.

ELLFISH file was created and a particular property varied while other parameters remained as the template value; the template used for these sweeps is listed in Appendix 5. The full set of results are listed in Appendices 5, 5, 5 and 5.

Figure 50 shows the transit time factor and maximum electric field on the cavity surface for different values of a_I/b_I. Reducing the value from 1.5 to 0.5 produces a 1 % reduction in the transit time factor and a 20 % reduction in peak electric field on the cavity surface. Appendix 5 shows an associated reduction in ZT^2 of only $\sim 2\,\%$. Similar reductions in the peak electric field could be obtained by varying the other parameters, but the resulting drop in the transit-time factor was larger. It was decided to investigate a geometry with a $\frac{a_I}{b_I} = 0.6$.

4.5.3 Other Parameters

Consideration for higher order modes motivated the value of R_b and a_I/b_I has been chosen for the impact on peak surface electric field. The remaining parameters, b_D, a_D/b_D and α_w are limited due to their impact on the transit-time factor. Of these parameters increasing a_D/b_D had the largest positive impact on ZT^2, E_{peak} and H_{peak} as shown by Figure 57 in comparison with Figures 56 and 58. A value of $a_D/b_D = 0.8$ was chosen, and the remaining parameters chosen to ensure that the transit-time factor remained above the required limit for a single-cell cavity.

4.6 Final Cavity

The geometric parameters of the final cavity design are listed in Table 12, the ELLFISH file is listed in Appendix 5 and an image of the cavity is shown in Figure 51. The resulting properties are compared with those of the prototype cavity in Table 13.

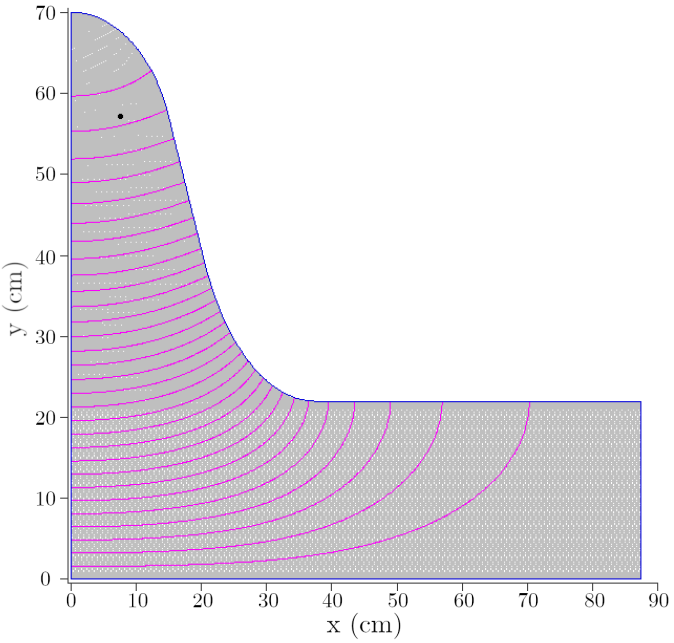

Figure 51: Final cavity geometry in SUPERFISH.

Property	Unit	Value
b_D	cm	20
a_D/b_D		0.8
α_w	degree	17
a_I/b_I		0.6
R_b	cm	22
D	cm	140.077
L	cm	74.84

Table 12: Geometric parameters of the final cavity.

Property	Unit	Final Cavity	Prototype Cavity
E_{acc}	(MV/m)	12	-
$E_{\text{peak}}/E_{\text{acc}}$		1.07	1.69
$B_{\text{peak}}/E_{\text{acc}}$	mT/(MV/m)	3.24	4.34
r/Q	Ω	106	121
Q		0.9×10^{10}	-
Transit Time Factor		0.617	-

Table 13: SUPERFISH output for final cavity design compared with the properties of the prototype muon cavity [40]; r/Q doubled from half-cell simulation.

4.6.1 CST Verification

To verify the parameters output by SUPERFISH the cavity was also simulated using the Eigenmode solver in CST Microwave Studio; see Figure 52a. Initially, the field on-axis was compared by scaling

the field for a given time-averaged, stored energy density

$$
\begin{aligned}
U_{CST} &= \frac{\varepsilon_0}{2} E_{CST}^2, \\
U_{SF} &= \frac{\varepsilon_0}{2} E_{SF}^2, \\
E_{SF} &= E_{cst} \sqrt{\frac{U_{SF}}{U_{CST}}},
\end{aligned} \tag{18}
$$

where U_{CST} the stored energy density in a CST Eigenmode simulation and U_{SF} is the stored energy density in the SUPERFISH simulation of the same cavity [48]; a similar formula can be derived for the magnetic field. Provided $U_{SF}(\vec{r}, t) = kU_{CST}(\vec{r}, t)$, where k is a constant the total energy can be used in place of the energy densities as the internal volumes are the same in both simulations. The total stored energy in a CST eigenmode simulation is 1 J, while the energy stored in a SUPERFISH simulation is determined from the field normalisation and can be obtained from the output SFO file. The full stored energy is twice that output from a half-cell simulation and in this case was 230.74 J. These numbers were inserted into Equation 18 and the on-axis electric field overlaid with the field from SUPERFISH; see Figure 53.

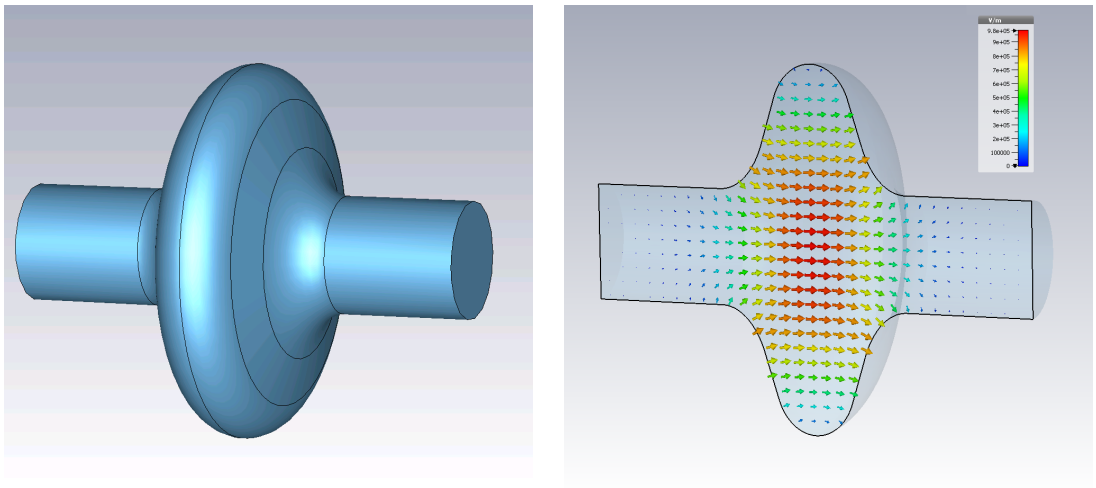

(a) (b)

Figure 52: (a) Geometry of the final cavity in CST Microwave Studio. (b) TM010 mode electric field.

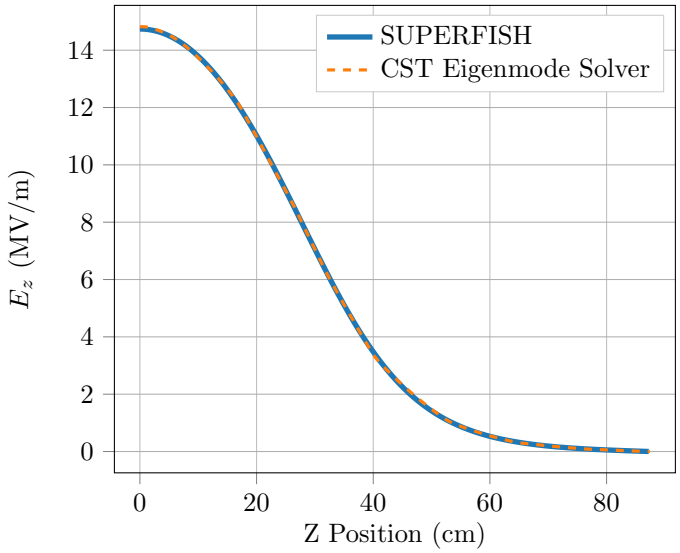

Figure 53: Electric field on-axis for a half-cell geometry from CST and SUPERFISH overlaid; CST field scaled with Equation (18).

The peak fields at the cavity surface were also evaluated using the following procedure:

1. Select one face of the geometry, e.g. the dome region
2. Create a new face from the navigation tree
3. Repeat for one half of the cavity
4. Run the Eigenmode simulation
5. Create a "Evaluate Field on Face" postprocessing step
6. Select the TM010 mode, evaluate the ABS component, export the maximum value and ensure "Evaluate on Surface" is selected
7. Repeat for each of the created faces
8. Evaluate the postprocessing steps and identify the largest field
9. Scale the field using Equation (18)

The resulting peak electric field is $E_{\text{peak}} = 12.78\,\text{MV}\,\text{m}^{-1}$, differing from the SUPERFISH value by 0.7 %. The resulting peak H field is $H_{\text{peak}} = 31.9\,\text{A}\,\text{m}^{-1}$ differing from the SUPERFISH value by 3 %.

The transit time factor was verified with the following process

1. Run simulation
2. Add postprocessing step "3D Eigenmode Result" and set the Result Value to voltage, choose the appropriate mode and integration direction, select the max range but ensure that "consider particle velocity" is **not** selected.
3. Duplicate the previous postprocessing step, but in this duplicate ensure "consider particle velocity" **is** selected and set an appropriate velocity; in this case 1.
4. Divide the result of the second postprocessing step by the result of the first in a "Mix Template Results" postprocessing step.

The value obtained was 0.617 , the same as the SUPERFISH value listed in Table 13 to the specified precision.

The r/Q factor, which depends only on the cavity geometry and transit time factor was obtained from a "3D Eigenmode Result" postprocessing step which gave the result of 106.7 Ω, differing from the SUPERFISH result by 0.7 %.

4.7 Outlook

Trapped HOMs remain an issue for this cavity and HOM couplers should be added to the simulation. If beam pipe aperture radius must be increased significantly then an symmetrical single cell, at 11 $\mathrm{MV\,m^{-1}}$ cavity would be unable to provide the required accelerating field. It is reasonable to assume that fields would not improve significantly beyond this limit of the prototype muon cavity. If aperture was to be made large only on one side then this could allow lower frequency HOMs to propagate whilst improving the transit-time factor [47]. If this cannot provide the necessary HOM suppression then more than one cavity would be required.

The tuning system would require significant research and development to satisfy the requirement of a 130 kHz bandwidth and a 370 $\mathrm{kHzs^{-1}}$ frequency swing rate. Similar bandwidths have been achieved elsewhere, such as the cavities LHC which has achieved 200 kHz on a 400 MHz resonant frequency and so this range does not seem implausible [39]. One example of a fast, high bandwidth tuning system based on the Lorentz forces between two superconducting coils was found which has the potential to satisfy all tuning requirements [42]; other options include a superconducting plunger [50].

The issue of cavity tuning would be improved provided the injection energy from the PS could be increased. With an injection energy of 50 GeV a bandwidth of only 36 kHz would be required; lower than the bandwidth of the 400 MHz LHC cavities [39]. The swing rate would also be reduced to 60 $\mathrm{kHzs^{-1}}$, which is still considered large. If the length of the injected bunches could also be reduced in such an upgrade then it seems possible that the RF frequency could be increased to 400 MHz which would reduce the cavity dimensions. This would have the advantage of existing experience with the LHC cavities, the reduced cost of niobium and a reduction in absolute beam pipe aperture which was limited in the prototype cavity to reduce the risk of vacuum leaks [40].

5 Conclusion

If the FCC-*hh* is to be built it will require a high energy booster. The scSPS is a promising option for this purpose due to its low complexity and running costs. Through the undertaking of this design project we were able to investigate and develop several of the key aspects of the design of the scSPS. We were able to show that the current design of the scSPS lattice satisfies the parameters needed for successful operation.

By performing chromaticity studies on this lattice we were able to quantify the strength of chromatic effects on the scSPS beam. We were able to calculate the number and the strength of sextupole magnets that would be required to correct these chromatic effects. The field strength of this sextupole was shown to be very small and easy to produce with current magnet technology.

The dispersion around the lattice was investigated, with several methods of dispersion suppression being considered. It was shown that using reduced field suppressor, singularly powered quadrupole and trimmer quadrupole suppressor schemes the dispersion in the long straight sections of the scSPS tunnel could be reduced to a very low value.

Other lattice designs were also investigated. It was shown that a lattice made of unit cells of a different length to the current scSPS lattice could be used if the scSPS magnets cannot perform as required for the original lattice.

To achieve the fast ramping rates required for the scSPS the use of similar superconducting Rutherford cables to the SIS300 accelerator was proposed. It was shown that a single layer of 11 mm wide cables of this design could provide the necessary dipole field for the scSPS when operating at a temperature of 1.9 K. However, the large aperture of the scSPS meant that single layer quadrupole magnets could not be produced using these cables.

It was, therefore, proposed to use wider 15 mm cables, again with a similar design to the SIS300 cables. For these cables it was shown that a single layered dipole and quadrupole designs, with a few alterations, could operate safely at 1.9 K. The field quality of each magnet was evaluated and was found to be close to the design goal, which may be reached with minor changes to the coil or yoke geometry.

As cryogenically cooling magnets to 1.9 K is both difficult and expensive, graded, two layer designs were produced for the dipole and quadrupole magnets. This would allow an investigation of whether the scSPS could operate at 4.2 K. The dipole design was shown to be able to operate safely at this temperature. However, the quadrupole design would require several changes, including a more aggressive coil grading to safely operate at 4.2 K.

Sextupole magnets were also designed for the scSPS. It was shown that resistive magnets would be able to provide sufficient correction of chromatic effects in the beam with liquid cooled wires. It was also shown that by using a superconducting sextupole design, much larger sextupole fields could be produced. The use of these magnets in the scSPS would allow the use of fewer sextupoles, thus saving lattice space for other equipment.

The fundamental RF parameters have been decided based on conditions imposed by the injected bunch, the FCC bunch spacing and the maximum number of bunches which can be safely transferred at one time to the FCC. The harmonic number will be 4605, producing an RF frequency of 200 MHz. The bunch structure was chosen to contain two trains of 320 bunches, separated by 25 ns and two 3.5 µs abort gaps.

Acceleration of protons from 26 GeV to 1.3 TeV in the scSPS requires a tuning range of 130 kHz. The frequency swing rate of 370 kHzs^{-1} is also large compared to typical high-bandwidth tuning systems.

After some consideration it was decided to investigate using a superconducting elliptical cavity. The primary advantages of this are the improved efficiency and the option to use larger beam pipe apertures compared to similar normal conducting cavities, which can improve beam stability. The cavity has a larger diameter than is typical for its kind, however such a cavity has been fabricated in the past for muon acceleration.

The design of the cavity geometry took into consideration the peak surface electric field, suppression of higher order modes and the more general optimisation of properties such as the shunt impedance and peak surface magnetic field. To address the issue of higher order modes a large aperture was chosen, however this was limited by the transit-time factor to be around 22 cm. To investigate the impact of geometrical parameters a series of parameter sweeps were performed in

SUPERFISH and the results discussed in Sections 4.5 and 4.5.3. These results allowed the surface surface electric field to be minimised by reducing a_I/b_I. The final cavity design was simulated in SUPERFISH and various parameters cross-checked with CST Eigenmode simulations in Sections 4.6 and 4.6.1. The two codes gave very similar results when scaling for the stored energy in the cavity, differing by less than $\sim$3 %.

Several further investigations could be performed into the design of the scSPS. Dispersion suppressor designs and chromaticity studies could be performed for each of the alternative lattice designs discussed in the report. More work could be undertaken to compare the advantages and disadvantages for the three dispersion suppressor options to choose the optimal design. Studies could be further performed on the arrangement of sextupole magnets in the scSPS lattice as well as their strength.

By altering the geometry of the magnets, the field quality and load margins could be increased, making the scSPS safer and more reliable, whilst providing a higher quality beam to the FCC-*hh*. By investigating AC losses around the injection field, we will be able to asses whether the current, 25 GeV, injection energy is viable. If not, it will be necessary to investigate injection from the PS2 at 50 GeV, with the costs associated with both injection options being assessed. All current work on magnet design has been done in 2D, 3D simulations must be done. The mechanical stresses must be evaluated for the magnets, particularly the superconducting ones, where they will be very high. Doing this will allow for the design of the magnet collars. The thermal properties of the magnets must be evaluated and specifically the operating temperature of the superconducting magnets. The costs of extra cryogenic cooling to lower temperatures must be weighed up against the extra costs caused by having more cables at higher temperatures. Any improvements to field quality and AC losses at different operating temperatures must also be investigated.

Due to the large aperture the problem of suppressing higher order modes is difficult. For further development of the 200 MHz cavity, methods of damping or trapping higher order modes must be developed. The use of asymmetric beam pipes could be investigated to improve the transit time factor, whilst also helping to suppress higher order modes. The method of increasing cut-off pipe apertures should also be investigated. Again the use of the PS2 as an injector to the scSPS should be investigated to allow the use of more mature 400 MHz cavities with a smaller frequency swing.

References

[1] M. Mangano et al., eds. *Future Circular Collider Study. Volume 1: Physics Opportunities. Conceptual Design Report*. CERN-ACC-2018-0056. Submitted for publication to Eur. Phys. J. C. 2018. URL: http://cds.cern.ch/record/2651294.

[2] F Burkart et al. "Conceptual Design Considerations For A 1.3 TeV Superconducting SPS (scSPS)". In: (2017), p. 4.

[3] O.S. Bruning et al. *LHC Design Report*. CERN Yellow Reports: Monographs. 2004. URL: http://cds.cern.ch/record/782076.

[4] ATLAS Collaboration. "Observation of a new particle in the search for the Standard Model Higgs boson with the ATLAS detector at the LHC". In: *Physics Letters B* 716.1 (2012), pp. 1–29.

[5] CMS Collaboration. "Observation of a new boson at a mass of 125 GeV with the CMS experiment at the LHC". In: *Physics Letters B* 716.1 (2012), pp. 30–61. ISSN: 0370-2693.

[6] M. Benedikt et al., eds. *Future Circular Collider Study. Volume 3: The Hadron Collider (FCC-hh) Conceptual Design Report*. CERN-ACC-2018-0058. Submitted for publication to Eur. Phys. J. ST. 2018. URL: http://cds.cern.ch/record/2651300.

[7] L S Stoel et al. "High Energy Booster Options for a Future Circular Collider at CERN". In: May 2016.

[8] *The 300 GeV programme*. Geneva: CERN, 1972. URL: https://cds.cern.ch/record/104068.

[9] V Hatton. "Operational history of the SPS collider 1981-1990". In: June 1991, 2952–2954 vol.5. DOI: 10.1109/PAC.1991.165151.

[10] *LEP design report*. Copies shelved as reports in LEP, PS and SPS libraries. Geneva: CERN, 1984. URL: https://cds.cern.ch/record/102083.

[11] M.A Green. *GESSS Machine Design Committee Reports*. 1972.

[12] Michael Benedikt. "Design Optimization of PS2". In: (Mar. 2019).

[13] B. J. Holzer. "Beam optics and lattice design for particle accelerators". In: (2013), pp. 19–20. URL: %7Bhttps://arxiv.org/abs/1303.6514%7D.

[14] H. Schopper, ed. *Advances of Accelerator Physics and Technologies*. vol 12. 1998.

[15] Helmut Wiedemann. *Particle accelerator physics; 3rd ed.* Berlin: Springer, 2007.

[16] Richard Carter. "Reviews of Accelerator Science and Technology: Volume 5 – Applications of Superconducting Technology to Accelerators, edited by Alexander W. Chao and Weiren Chou". In: *Contemporary Physics* 56 (Jan. 2015), pp. 1–2. DOI: 10.1080/00107514.2015.1005681.

[17] L Bottura. "A Practical Fit for the Critical Surface of NbTi". In: *IEEE Trans. Appl. Supercond.* 10.LHC-Project-Report-358. CERN-LHC-Project-Report-358. 1 (Dec. 1999), 1054–7. 5 p.

[18] Guenther Rosner. "Future Facility: FAIR at GSI". In: *Nuclear Physics B - Proceedings Supplements* 167 (2007). Proceedings of the 7th International Conference on Hyperons, Charm and Beauty Hadrons, pp. 77–81. ISSN: 0920-5632. DOI: https://doi.org/10.1016/j.nuclphysbps.2006.12.089. URL: http://www.sciencedirect.com/science/article/pii/S0920563206010516.

[19] H. Mueller et al. "Next Generation of Fast-Cycled Dipoles for SIS300 Synchrotron". In: *IEEE Transactions on Applied Superconductivity* 24.3 (June 2014), pp. 1–4. ISSN: 1051-8223. DOI: 10.1109/TASC.2013.2287635.

[20] S Kozub et al. "SIS 300 Fast-Cycling Superconducting Quadrupole Prototype". In: *IEEE Transactions on Applied Superconductivity - IEEE TRANS APPL SUPERCONDUCT* 22 (June 2012), pp. 4001104–4001104. DOI: 10.1109/TASC.2011.2174542.

[21] J Kaugerts et al. “Design of a 6 T, 1T/s fast-ramping Synchrotron magnet for GSI’s planned SIS 300 accelerator”. In: *Applied Superconductivity, IEEE Transactions on* 15 (July 2005), pp. 1225–1227. DOI: 10.1109/TASC.2005.849537.

[22] *6 T Dipole for the SPS Upgrade*. FCC Week. 2017.

[23] *6 T Pulsed Dipole for the SPS Upgrade*. FCC Week. 2018.

[24] Attilio Milanese. “An introduction to Magnets for Accelerators”. John Adams Institute Accelerator Course. 2017. URL: https://indico.cern.ch/event/590390/contributions/2381025/attachments/1401281/2140074/JAI_course_Jan_2017.pdf.

[25] “Stacks of SPS Dipole Magnets”. Sept. 1974. URL: http://cds.cern.ch/record/916909.

[26] *Opera Simulation Suite*. 2019. URL: operafea.com/opera-2d-and-opera-3d-for-machines/.

[27] R. C. Bossert et al. “Development of TQC01, a 90-mm Nb_3Sn model quadrupole for LHC upgrade based on SS collar.” In: *IEEE Trans. Appl. Supercond.* 16.2 (2006), pp. 370–373. DOI: 10.1109/TASC.2006.871320.

[28] G Dome and Radio Frequency Group. “The SPS Acceleration System”. In: *Proton Linear Accelerator Conference*. Vol. 2. 1976, pp. 138–147.

[29] D. Boussard et al. “The LHC superconducting cavities”. In: *Proceedings of the 1999 Particle Accelerator Conference (Cat. No.99CH36366)*. 1999 Particle Accelerator Conference. Vol. 2. New York, NY, USA: IEEE, 1999, pp. 946–948. ISBN: 978-0-7803-5573-6. DOI: 10.1109/PAC.1999.795409. URL: http://ieeexplore.ieee.org/document/795409/ (visited on 02/17/2019).

[30] *, howpublished = https://www.lhc-closer.es/taking_a_closer_look_at_lhc/0.rf_cavities, note = Accessed: 01-02-2019.*

[31] *Poisson Superfish*. https://laacg.lanl.gov/laacg/services/download_sf.phtml. Accessed: 01-11-2018.

[32] M.T. Menzel and H.K. Stokes. “User‘s guide for the POISSON/SUPERFISH Group of Codes”. In: (Jan. 1987). DOI: 10.2172/10140823.

[33] *CST MicroWave Studio*. https://www.cst.com/products/csts2. Accessed: 24-01-2019.

[34] Holger Podlech. “Superconducting versus normal conducting cavities”. In: *Proceedings, CERN Accelerator School on High Power Hadron Machines (CAS 2011): Bilbao, Spain, May 24-June 02, 2011*. 2013. DOI: 10.5170/CERN-2013-001.151. arXiv: 1303.6552 [physics.acc-ph].

[35] Alternative Triplet. “Contents of the machine design chapter for the long CDR”. In: (), pp. 1–44.

[36] S. Y. Lee. *Accelerator Physics*. 3rd Revised edition edition. Hackensack, NJ: Wspc, Nov. 16, 2011. 554 pp. ISBN: 978-981-4374-94-1.

[37] CHAO ALEXANDER WU ET AL. *HANDBOOK OF ACCELERATOR PHYSICS AND ENGINEERING*. 2nd Revised edition edition. Hackensack, New Jersey: World Scientific, May 25, 2013. 848 pp. ISBN: 978-981-4417-17-4.

[38] P Schmüser. “Basic principles of RF superconductivity and superconducting cavities”. In: (2006). URL: http://cds.cern.ch/record/941325.

[39] Joachim Tuckmantel. “NEW RF SYSTEMS FOR THE SUPER-SPS AND SUPER-ISR”. In: (), p. 12.

[40] R L Geng et al. “200 MHz Nb-Cu Cavities for Muon Acceleration”. In: (), p. 4.

[41] O. Kugeler. “Cavity Tuners”. In: Presented at the Energy Recovery Linac Workshop, Cornell University, NY, 2009.

[42] V. Kashikhin et al. “Electromagnetic SCRF Cavity Tuner”. In: *Particle accelerator. Proceedings, 23rd Conference, PAC’09, Vancouver, Canada, May 4-8, 2009*. 2010, MO6PFP056. URL: http://lss.fnal.gov/archive/2009/conf/fermilab-conf-09-165-td.pdf.

[43] Y. M. Li et al. *MultiPac 2.1 - Multipacting Simulation Package with a 2D FEM Field Solver for a Microsoft Windows System*. CERN Document Server. 2008. URL: https://cds.cern.ch/record/1182118 (visited on 03/19/2019).

[44] G V Romanov. "Simulation of Multipacting in HINS Accelerating Structures with CST Particle Studio". In: *Computer Simulation* (), p. 3.

[45] B Bonin. "FIELD EMISSION IN RF CAVITIES". In: (), p. 10.

[46] J. Graber et al. "Reduction of field emission in superconducting cavities with high power pulsed RF". In: *Nuclear Instruments and Methods in Physics Research Section A: Accelerators, Spectrometers, Detectors and Associated Equipment* 350.3 (Nov. 1, 1994), pp. 572–581. ISSN: 0168-9002. DOI: 10.1016/0168-9002(94)91260-2. URL: http://www.sciencedirect.com/science/article/pii/0168900294912602 (visited on 03/19/2019).

[47] T Furuya et al. "Superconducting Accelerating Cavity for KEK B-Factory". In: (1995), p. 5.

[48] David M. Pozar. *Microwave Engineering*. 4th Edition edition. Hoboken, NJ: John Wiley & Sons, Dec. 23, 2011. 752 pp. ISBN: 978-0-470-63155-3.

[49] Michael Benedikt. *The PS Complex as Proton Pre-Injector for the LHC Design and Implementation Report*. URL: http://blas.web.cern.ch/blas/Publications/2000-03.pdf (visited on 03/14/2019).

[50] D. Longuevergne et al. "An innovative tuning system for superconducting accelerating cavities". In: *Nuclear Instruments and Methods in Physics Research Section A: Accelerators, Spectrometers, Detectors and Associated Equipment* 749 (June 11, 2014), pp. 7–13. ISSN: 0168-9002. DOI: 10.1016/j.nima.2014.02.046. URL: http://www.sciencedirect.com/science/article/pii/S0168900214002277 (visited on 02/22/2019).

Appendices

A. HOM Supression in a Pillbox

A cylindrical cavity of radius R_c and length d_c has two axially aligned cylindrical waveguide apertures as shown in Figure 54. In order to suppress the affect of HOMs all modes except the TM010 mode should become propagating above the cut-off frequency of the adjoining apertures. In this way, these HOM's will be able to propagate out of the cavity while the accelerating mode remains resonant.

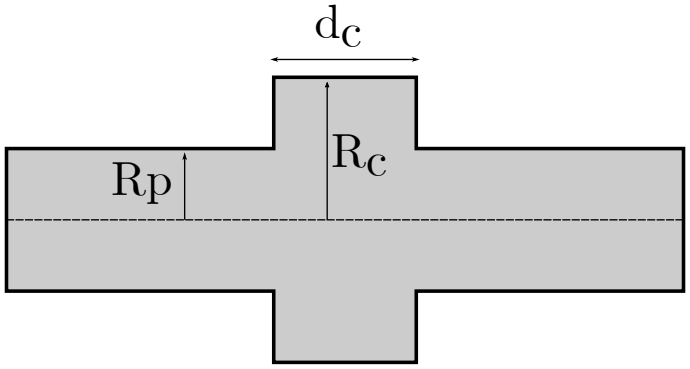

Figure 54: A cylindrical pillbox of radius R_c and length d_c with two apertures of radius R_p.

Figure 55 shows a chart of resonant modes which can exist within a cylindrical waveguide cavity. This shows that the frequencies at which higher order modes occur depend on the geometry of the cavity. Provided $(2a/d)^2$ is such that the first HOM is the TM110 mode then the cutoff frequency is given by

$$f_{TM110} = \frac{c}{2\pi}\frac{p_{11}}{R_c}, \tag{19}$$

where p_{11} is the first zero of a first order Bessel function of the first kind. The lowest frequency propagating mode in a cylindrical waveguide is the TE11 mode, with a cut-off frequency of

$$f_{c,TE11} = \frac{c}{2\pi}\frac{p'_{11}}{R_p}, \tag{20}$$

where c is the speed of light in a vacuum and p'_{11} is the first zero of the first derivative of a Bessel function of the first kind [48]. Neglecting the affects that adding an aperture to the cavity could have on the resonant frequency of a given mode, and the coupling efficiency between these modes, it is required that for the TM011 mode to propagate $f_{c,TM011} > f_{c,TE11}$,

$$R_p > \frac{p'_{11}}{p_{11}}R_c, \tag{21}$$

$$\gtrapprox 0.5R_c. \tag{22}$$

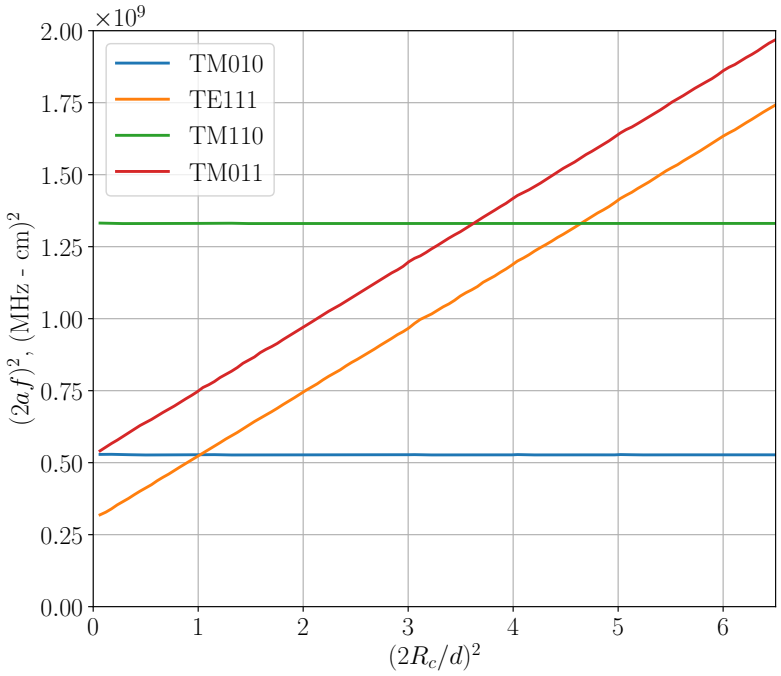

Figure 55: Resonant mode chart for a cylindrical cavity (adapted), [48].

B. Aperture Radius Parameter Sweep ELLFISH Template

```
Title
Resonant frequency = 200 MHz
ENDTitle

PARTICLE                H+
SUPERConductor          4   9.2   1.0E-08

NumberOfCells           1     ; used by the ELLCAV code
HALF_cavity

FILEname_prefix         REPLACE
SEQuence_number         1
FREQuency               200.08
BETA                    0.999
LENGTH                  74.84322909386
DIAMeter                130.8402446811
E0_Normalization        12
DOME_B                  15
LEFT_DOME_B             15
RIGHT_DOME_B            15
DOME_A/B                0.7
LEFT_DOME_A/B           0.7
RIGHT_DOME_A/B          0.7
WALL_Angle              15
LEFT_Wall_angle         15
RIGHT_Wall_angle        15
EQUATOR_flat            0.0
LEFT_Equator_flat       0.0
RIGHT_Equator_flat      0.0
IRIS_flat               0.0
LEFT_Iris_flat          0.0
RIGHT_Iris_flat         0.0
RIGHT_BEAM_tube         70.0
IRIS_A/B                1.0
LEFT_IRIS_A/B           1.0
RIGHT_IRIS_A/B          1.0
BETASTART               0.0
BETASTOP                0.0
BETASTEP                0.0
BETATABLE               0.0
BORE_radius             30
SECOND_Beam_tube        0.0
SECOND_TUBE_Radius      0.0
DELTA_frequency         0.01
MESH_size               0.2
INCrement               2
START                   2

EndFile
```

C. Parameter Sweep: ELLFISH Template

```
Title
Resonant frequency = 200 MHz
ENDTitle

PARTICLE                H+
SUPERConductor          4   9.2   1.0E-08

NumberOfCells           1     ; used by the ELLCAV code
HALF_cavity

FILEname_prefix         REPLACE
SEQuence_number         1
FREQuency               200.08
BETA                    0.999
LENGTH                  74.84322909386
DIAMeter                130.8402446811
E0_Normalization        12
DOME_B                  22
LEFT_DOME_B             22
RIGHT_DOME_B            22
DOME_A/B                0.7
LEFT_DOME_A/B           0.7
RIGHT_DOME_A/B          0.7
WALL_Angle              20
LEFT_Wall_angle         20
RIGHT_Wall_angle        20
EQUATOR_flat            0.0
LEFT_Equator_flat       0.0
RIGHT_Equator_flat      0.0
IRIS_flat               0.0
LEFT_Iris_flat          0.0
RIGHT_Iris_flat         0.0
RIGHT_BEAM_tube         50.0
IRIS_A/B                0.75
LEFT_IRIS_A/B           0.75
RIGHT_IRIS_A/B          0.75
BETASTART               0.0
BETASTOP                0.0
BETASTEP                0.0
BETATABLE               0.0
BORE_radius             22
SECOND_Beam_tube        0.0
SECOND_TUBE_Radius      0.0
DELTA_frequency         0.01
MESH_size               0.2
INCrement               2
START                   2

EndFile
```

D. Parameter Sweep: Dome B Results

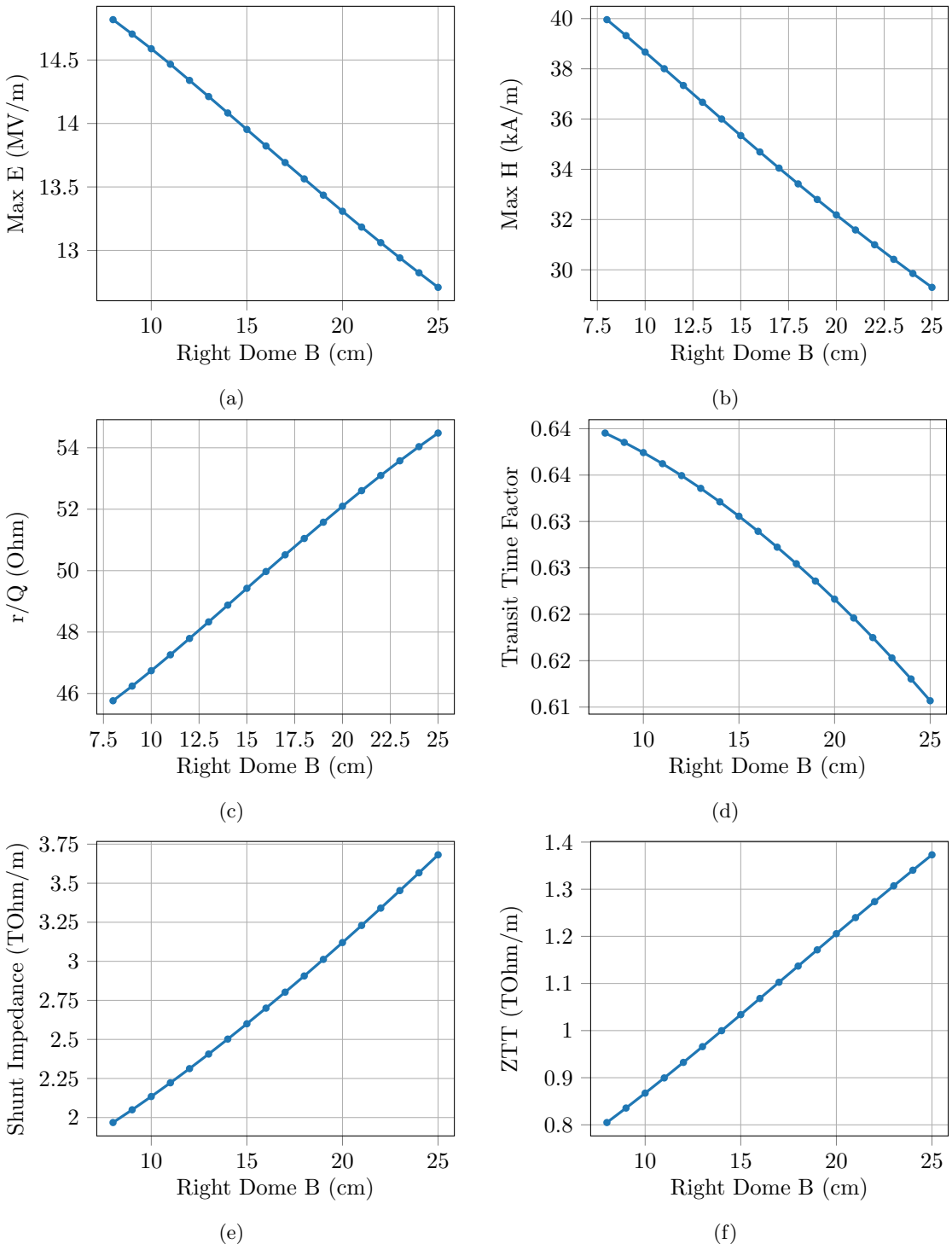

Figure 56: Results from half-cavity ELLFISH simulations where property b_D was varied; note that r/Q is half of the full cavity value.

E. Parameter Sweep: Dome A/B Results

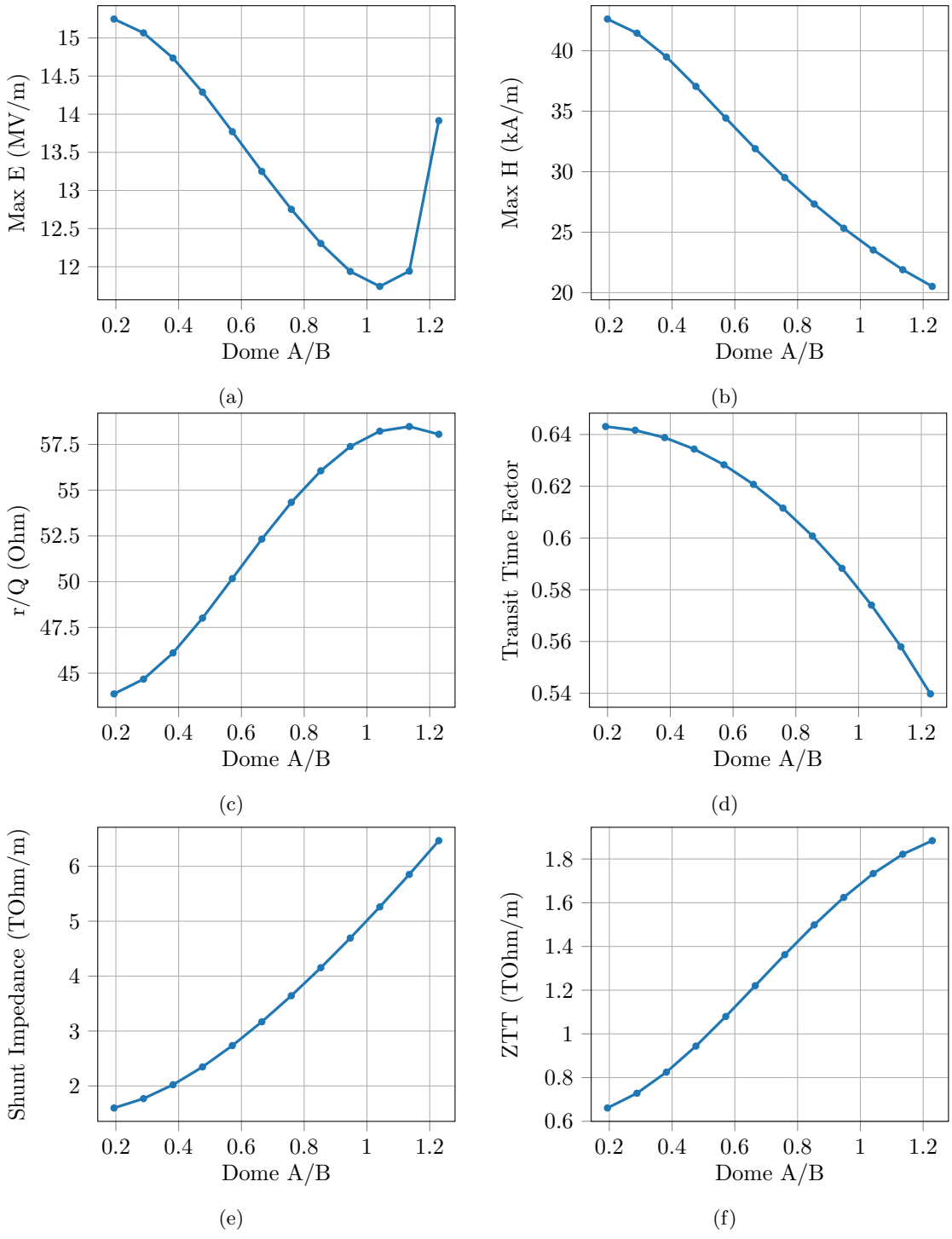

Figure 57: Results from half-cavity ELLFISH simulations where property a_D/b_D was varied; note that r/Q is half of the full cavity value.

F. Parameter Sweep: Wall Angle Results

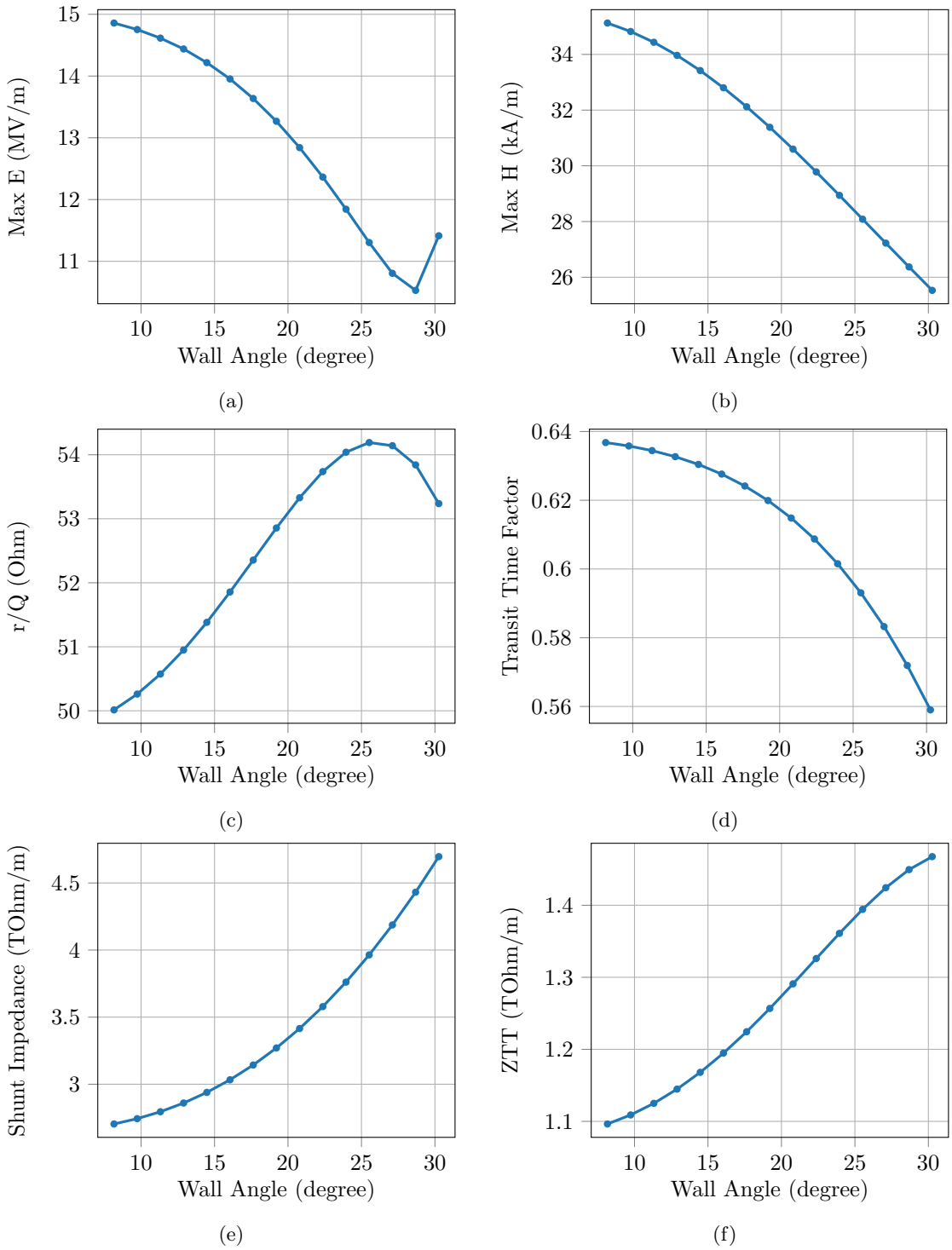

Figure 58: Results from half-cavity ELLFISH simulations where property α_W was varied; note that r/Q is half of the full cavity value.

G. Parameter Sweep: Iris A/B Results

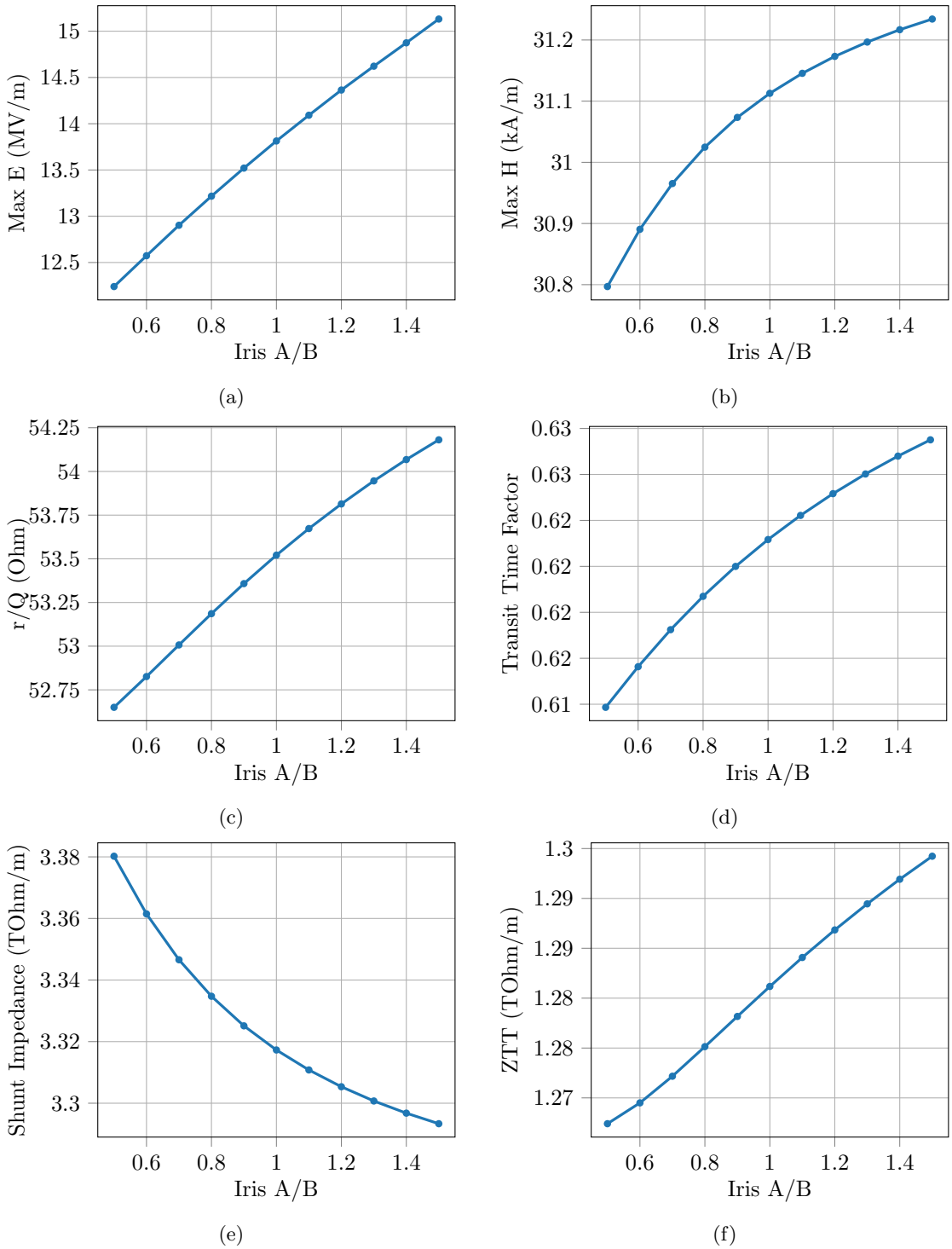

Figure 59: Results from half-cavity ELLFISH simulations where property a_I/b_I was varied; note that r/Q is half of the full cavity value.

H. Final Cavity ELLFISH Input

```
Title
Resonant frequency = 200 MHz
ENDTitle

PARTICLE                H+
SUPERConductor          4   9.2   1.0E-08

NumberOfCells           1     ; used by the ELLCAV code
HALF_cavity

FILEname_prefix         FINAL_CAVITY
SEQuence_number         1
FREQuency               200.08
BETA                    0.999
LENGTH                  74.84322909386
DIAMeter                140.0766845384
E0_Normalization        12
E0T_Normalization       7.409288326213
DOME_B                  20
LEFT_DOME_B             20
RIGHT_DOME_B            20
DOME_A/B                0.8
LEFT_DOME_A/B           0.8
RIGHT_DOME_A/B          0.8
WALL_Angle              17
LEFT_Wall_angle         17
RIGHT_Wall_angle        17
EQUATOR_flat            0.0
LEFT_Equator_flat       0.0
RIGHT_Equator_flat      0.0
IRIS_flat               0.0
LEFT_Iris_flat          0.0
RIGHT_Iris_flat         0.0
RIGHT_BEAM_tube         50
IRIS_A/B                0.6
LEFT_IRIS_A/B           0.6
RIGHT_IRIS_A/B          0.6
BETASTART               0.0
BETASTOP                0.0
BETASTEP                0.0
BETATABLE               0.0
BORE_radius             22
LEFT_BORE_radius        22
RIGHT_BORE_radius       22
SECOND_Beam_tube        0.0
SECOND_TUBE_Radius      0.0
DELTA_frequency         0.01
MESH_size               0.2
INCrement               2
START                   -2

EndFile
```